CHAPTER 7

PRESSURE TEMPERATURE CONDITIONS OF METAMORPHISM

7.1. INTRODUCTION

Microprobe analyses were carried out on two samples of garnet-biotite schist of the study area with the aim of (a) measuring the chemical composition of the various constituent minerals, (b) detecting the zoning pattern in garnet and (c) using the microprobe data for calculating the P-T conditions of metamorphism. The microprobe measurements were carried out with the *CAMECA SX51 Microprobe* at the *Mineralogisches Institut, Heidelberg* with a high voltage of 15 kV and beam current of 20 mA. Two samples - one from Anjavana and the other from Lunavada were analyzed. Point analysis of the following minerals were made.

1. Core of garnet porphyroblast.
2. Rim of garnet porphyroblast in contact with biotite (D_2)
3. D_1 biotite.
4. Rim of D_2 biotite porphyroblast in contact with garnet porphyroblast.
5. Plagioclase inclusions in garnet.
6. Plagioclase in the matrix.
7. Opaque minerals (ilmenite inclusions) in garnet.
8. Opaque minerals (ilmenite) in the matrix.
9. Muscovite along S_1 foliation.
10. Muscovite along S_2 foliation

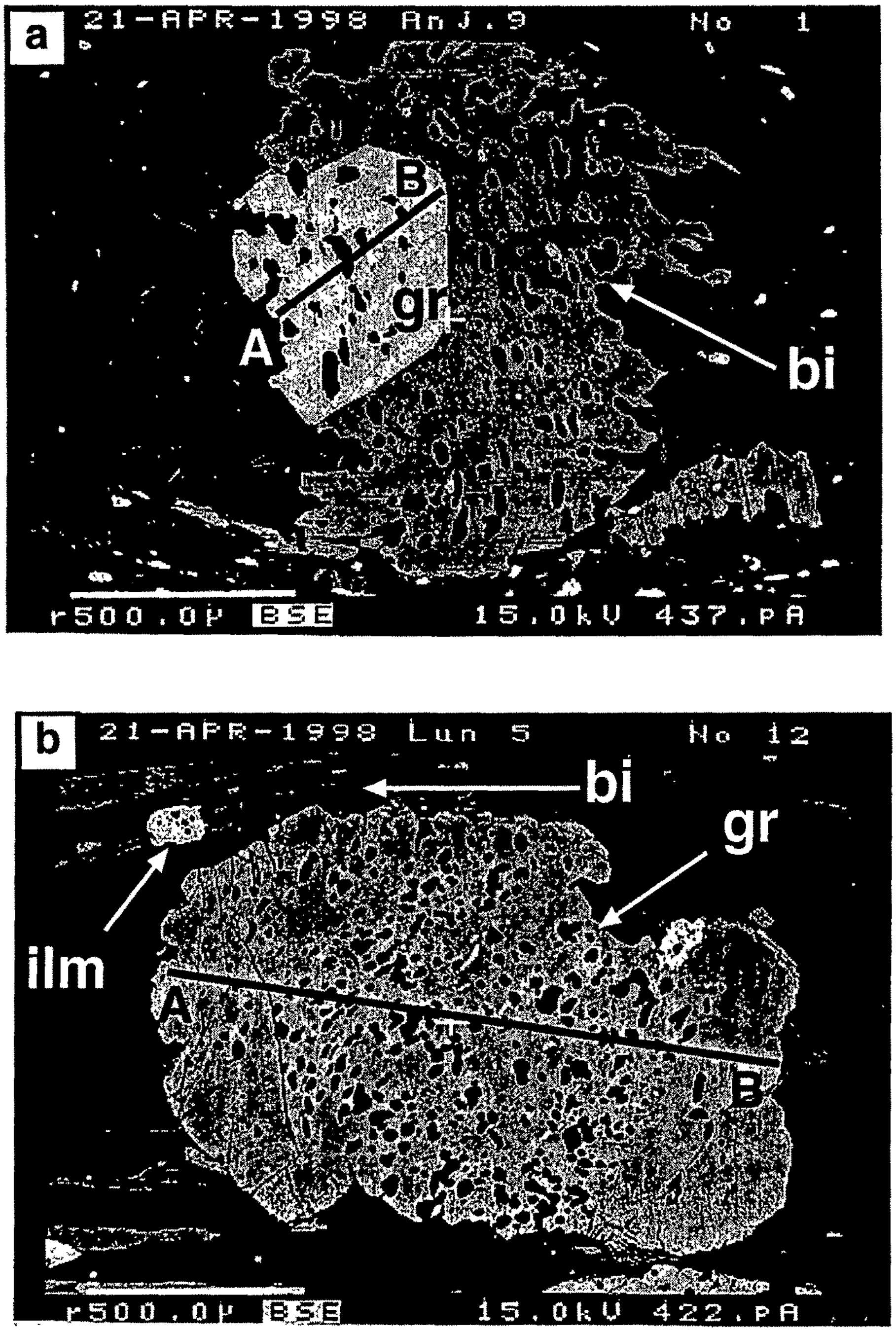

Fig. 7.1. Back Scattered Emission (BSE) images of the garnet porphyroblasts analyzed using the microprobe. (a) is the Anjavana sample and (b) is the Lunavada sample. Line AB represents the traverse made with the microprobe. ***bi*** is biotite, ***ilm*** is ilmenite and ***gr*** is garnet.

The representative analyses for the above minerals in the Anjavana and Lunavada sample are shown in Tables 7.1 and 7.2. It may be noted that the garnet porphyroblasts in the schists are syntectonic with D_2 deformation (as established in chapter 6).

7.2. ZONING IN GARNET

A few garnet crystals were subjected to line traverses to get information about the zoning pattern preserved within them. Fig. 7.1 shows the garnets for which traverses were made using the microprobe.

7.2.1. Zoning in garnets of the Anjavana sample

Garnet from the Anjavana sample were subjected to line traverses to get information about the zoning pattern preserved within them. Zoning is very conspicuously observed within the garnets. Fe, Mg, Mn and Ca are strongly zoned. This is clearly seen in the zoning profile in Fig. 7.2 and also in the X-ray maps showing the distribution of the above elements in two dimension (Fig. 7.3). It is observed in the zoning profile that XFe (almandine) increases from core to rim, XMn (spessartine) decreases from core to rim, XCa (grossularite) remains generally unzoned except for a slight decrease at the rims and XMg (pyrope) increases slightly towards the rim. The most characteristic profile is that for Mn (Fig. 7.2) which shows a typical bell-shape. This is interpreted to be typical of growth zoning in greenschist and amphibolite facies rocks (Tracy et al. 1976; Yardley, 1977; Spear, 1993, p.578). Accordingly, the zoning in the garnet presently under investigation is interpreted to be growth zoning i.e. it occurs as

Table7.1. Representative microprobe analyses from the Anjavana sample

	Garnet (core)	*Garnet (rim)*	*Biotite (S_1)*	*Biotite (S_2)*	*Muscovite (S_1)*	*Muscovite (S_2)*	*ilmenite (inclusion)*	*ilmenite Matrix*	*Feldspar (matrix)*
Code Nr.	***anj1-1***	***anj1-13***	***anj1.2-1***	***anj9-18***	***anj8-15***	***anj8-14***	***anj9g-2***	***anj9g-1***	***anj9fs-3***
SiO_2	36.86	36.58	35.32	35.15	45.81	46.84	0.02	0.01	63.06
TiO_2	0.21	0.02	1.48	1.39	0.29	0.32	47.48	48.49	0.00
Al_2O_3	19.69	19.98	17.24	15.63	30.34	29.13	0.00	0.00	23.89
Cr_2O_3	0.02	0.03	0.01	0.05	0.03	0.00	0.00	0.00	0.00
Fe_2O_3	0.00	0.00	0.00	0.00	0.00	0.00	8.81	4.86	0.00
FeO	23.55	34.33	20.83	20.01	2.73	2.47	40.29	42.20	0.00
MnO	13.49	4.65	0.05	0.00	0.03	0.00	1.66	1.24	0.00
NiO	0.00	0.00	0.00	0.00	0.00	0.00	0.00	0.00	0.00
MgO	1.11	2.25	9.54	9.58	0.74	1.07	0.37	0.00	0.00
CaO	4.86	1.79	0.01	0.00	0.00	0.00	0.06	0.01	4.35
Na_2O	0.01	0.02	0.26	0.25	1.00	0.96	0.00	0.00	9.24
K_2O	0.01	0.05	8.60	9.03	9.35	9.35	0.00	0.05	0.08
H_2O	0.00	0.00	3.84	3.74	4.25	4.26	0.00	0.00	0.00
Total	99.80	99.68	97.19	94.82	94.58	94.40	98.69	96.86	100.62

Table 7.2. Representative microprobe analyses from the Lunavada sample

	Garnet (core)	*Garnet (rim)*	*Biotite (S_1)*	*Biotite (S_2)*	*Muscovite (S_2)*	*ilmenite (inclusion)*	*ilmenite (matrix)*	*Feldspar (inclusion)*	*Feldspar (matrix)*
Code Nr.	***lun7-1***	***lun7-12***	***lun11-1***	***lun11-2***	***lun11-3***	***l-new-g-4***	***lun7-g-3***	***luna-fs-1***	***luna-fs-2***
SiO_2	36.56	36.64	34.93	34.93	45.79	0.06	0.00	67.47	62.65
TiO_2	0.03	0.03	1.48	1.63	0.50	51.10	52.01	0.00	0.00
Al_2O_2	19.97	20.22	16.76	17.00	31.56	0.00	0.00	20.46	22.95
Cr_2O_3	0.03	0.03	0.07	0.03	0.00	0.00	0.02	0.00	0.00
Fe_2O_3	0.00	0.00	0.00	0.00	0.00	0.42	0.12	1.58	1.19
FeO	36.45	37.30	21.04	20.83	0.99	44.93	45.93	0.00	0.00
MnO	2.10	1.50	0.04	0.08	0.03	0.94	0.78	0.00	0.00
NiO	0.00	0.00	0.00	0.00	0.00	0.00	0.00	0.00	0.00
MgO	2.49	2.20	8.57	8.26	0.52	0.02	0.01	0.00	0.00
CaO	2.46	1.89	0.00	0.00	0.00	0.07	0.00	0.59	1.91
Na_2O	0.00	0.02	0.16	0.19	1.23	0.00	0.00	10.72	8.57
K_2O	0.02	0.02	8.60	8.53	8.92	0.01	0.00	0.87	2.20
H_2O	0.00	0.00	3.76	3.76	4.27	0.00	0.00	0.00	0.00
Total	100.10	99.86	95.41	95.24	93.82	97.55	98.87	101.68	99.46

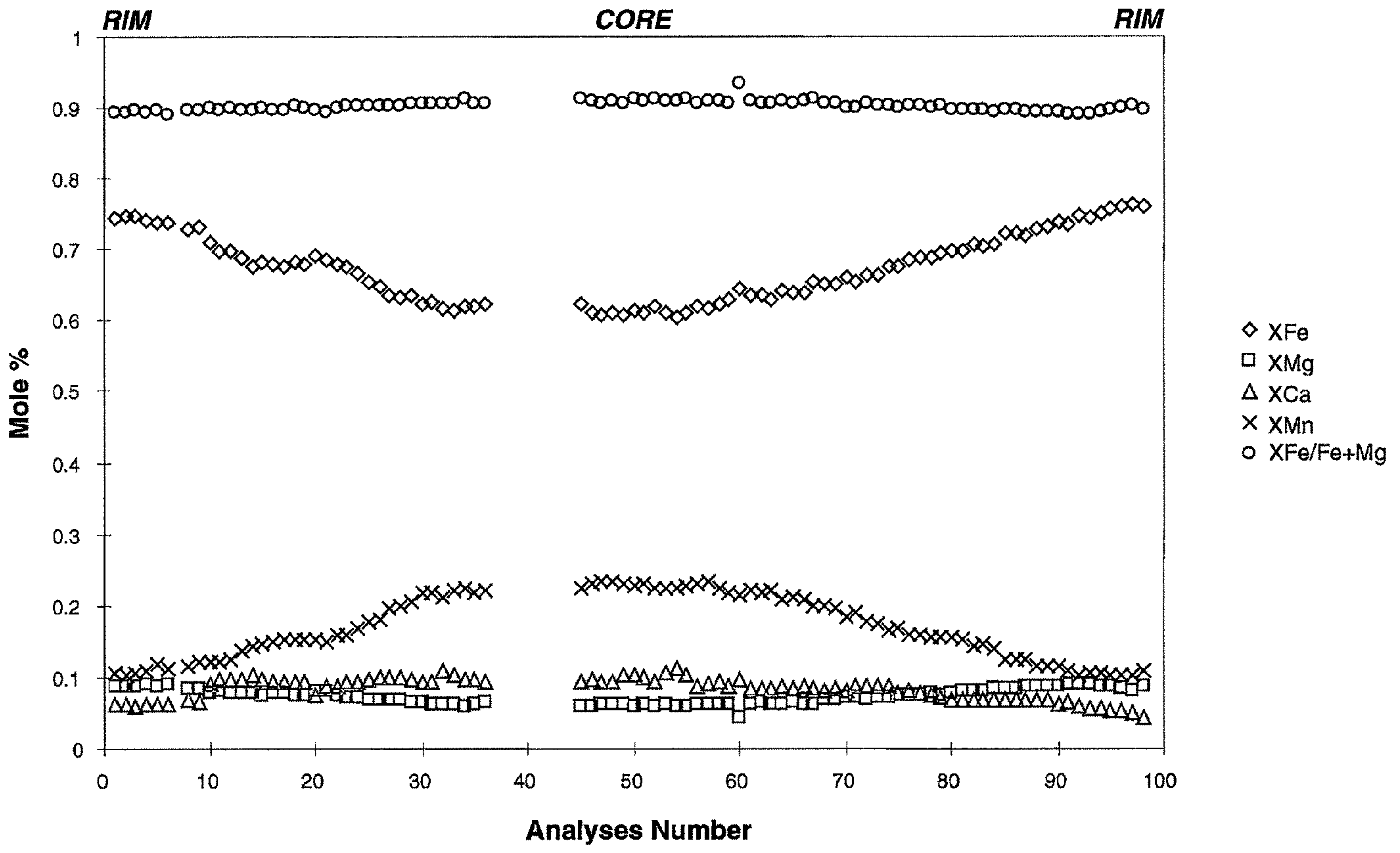

Fig. 7.2 . Zoning profile recorded in garnet from Anjavana sample. Total number of measurements = 98. Length of the profile line = 400µm

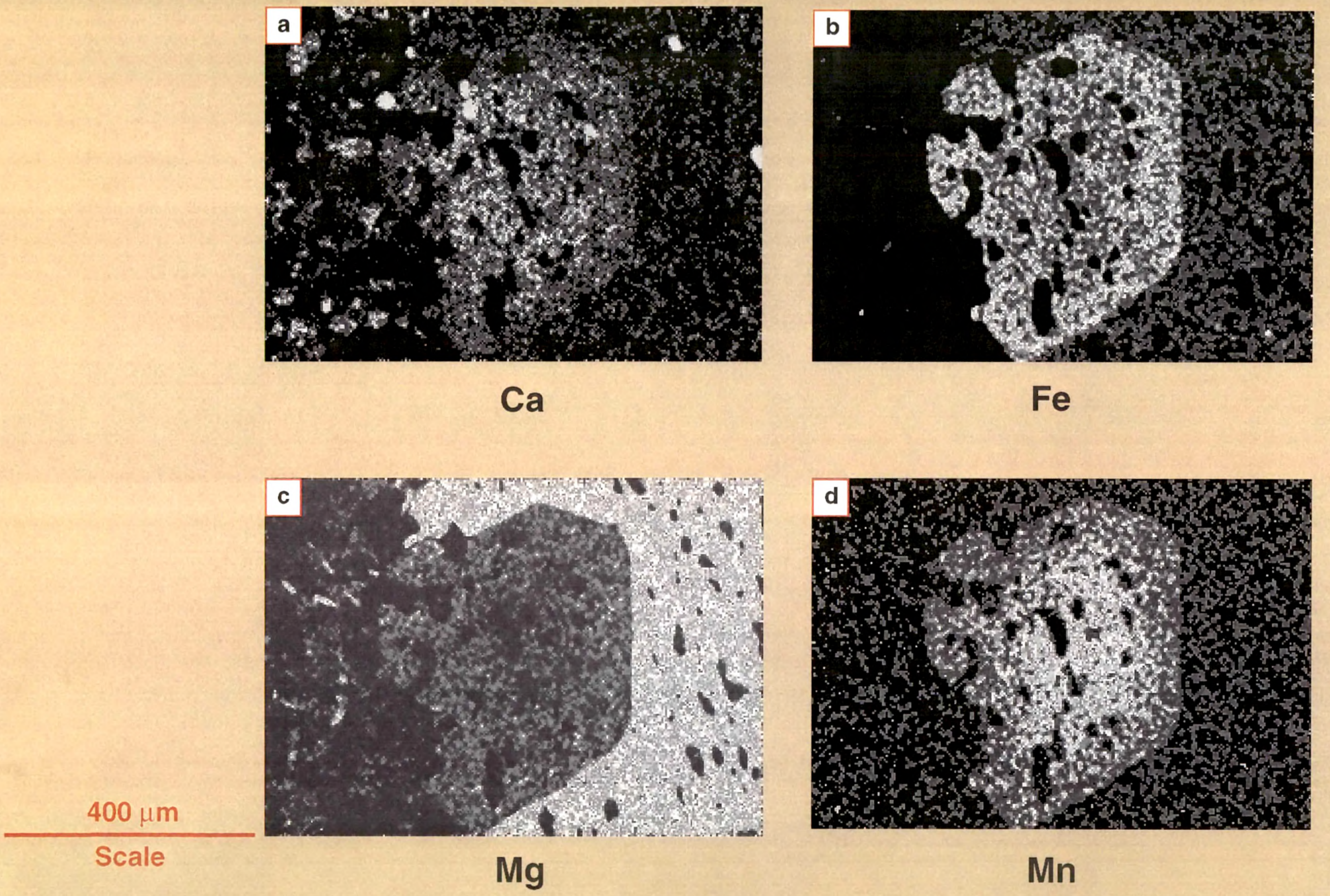

Fig. 7.3 . X-ray maps for (a) Ca, (b) Fe, (c) Mg and (d) Mn in garnet from Anjavana sample.

new shells of different composition are successively added onto the growing crystal. An important thing to be highlighted is the relatively unzoned nature of the Fe/Fe+Mg profile. This is an indication of the fact that the change in temperature during garnet growth was small (Spear, 1993, p. 633).

This is [illegible] of [illegible] plutonic garnet [illegible] core [illegible]

7.2.2. Zoning in garnets of Lunavada sample

In comparison to the strongly zoned Anjavana sample, the Lunavada sample is relatively unzoned (Fig. 7.4, 7.5). However, the zoning profiles for Fe, Fe/Fe+Mg and Mn show a increase at the rims of the garnet. Conversely, there is a decrease in the Mg content at the rim. These are indications of diffusion having been active during the cooling history of the sample. In other words, this is an indication of some retrogressive metamorphism subsequent to the achievement of peak metamorphic conditions (Yardley, 1977; Spear, 1993). The zoning profiles indicate that diffusion affected the compositions close to the rims of the garnet and did not penetrate to the core. This is interpreted from the fact that the growth zoning part is still preserved in the Fe and Mn profiles for the core of the garnet. The preservation of growth zoning in the core and diffusion zoning at the rims together give a “bird-wing” like appearance to the Fe and Mn profiles.

On the basis of above evidences has been concluded that diffusion affected/modified the rim composition of the garnet and did not cause any change in the core of the garnet. Moreover, there was no significant change in the temperature during garnet growth because the Fe/Fe+Mg profile is almost straight except at the rim.

In relation [illegible] [illegible] [illegible]

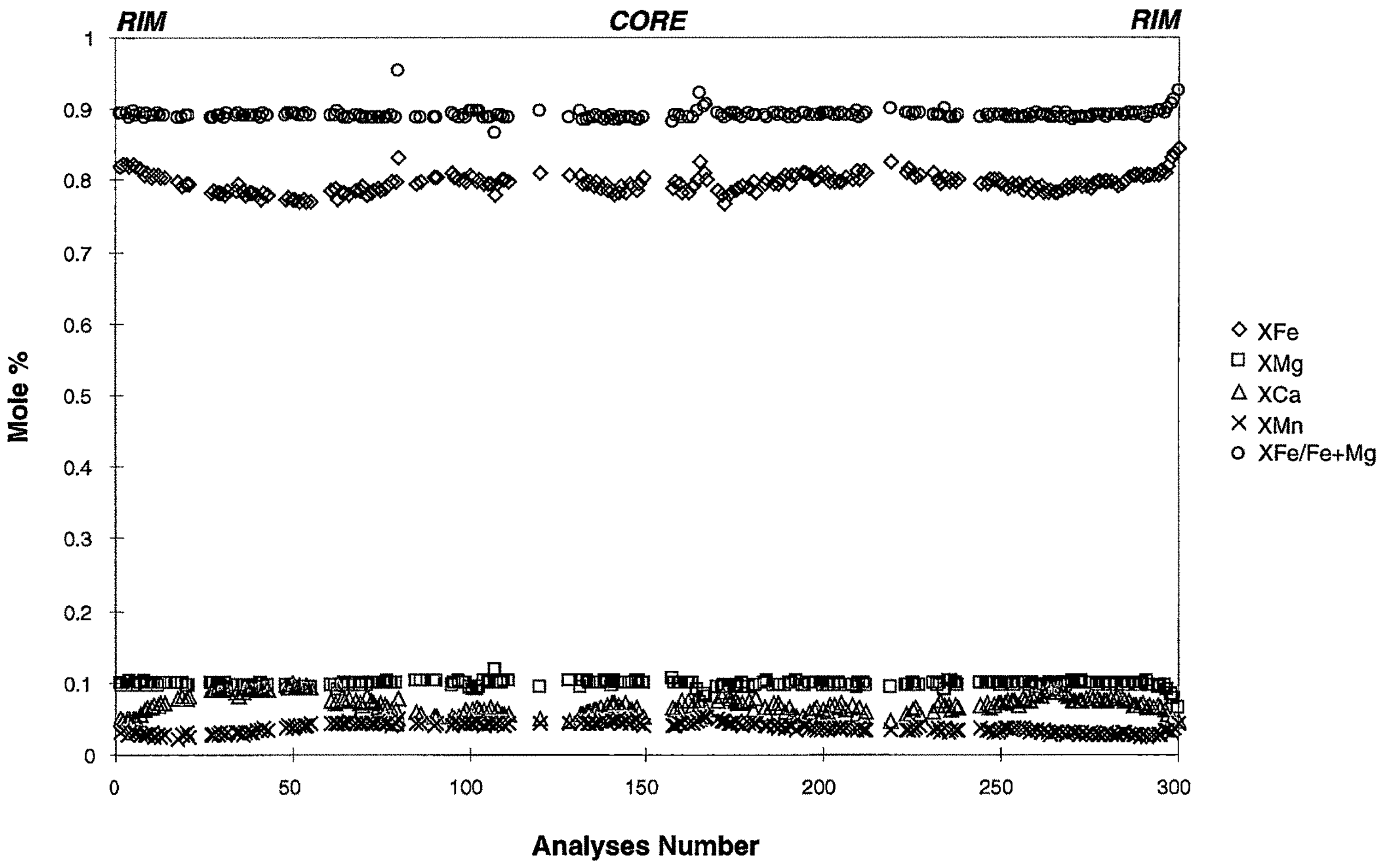

Fig. 7.4 . Zoning profile recorded in garnet from Lunavada sample. Total number of measurements = 300. Length of the profile line = 1500µm

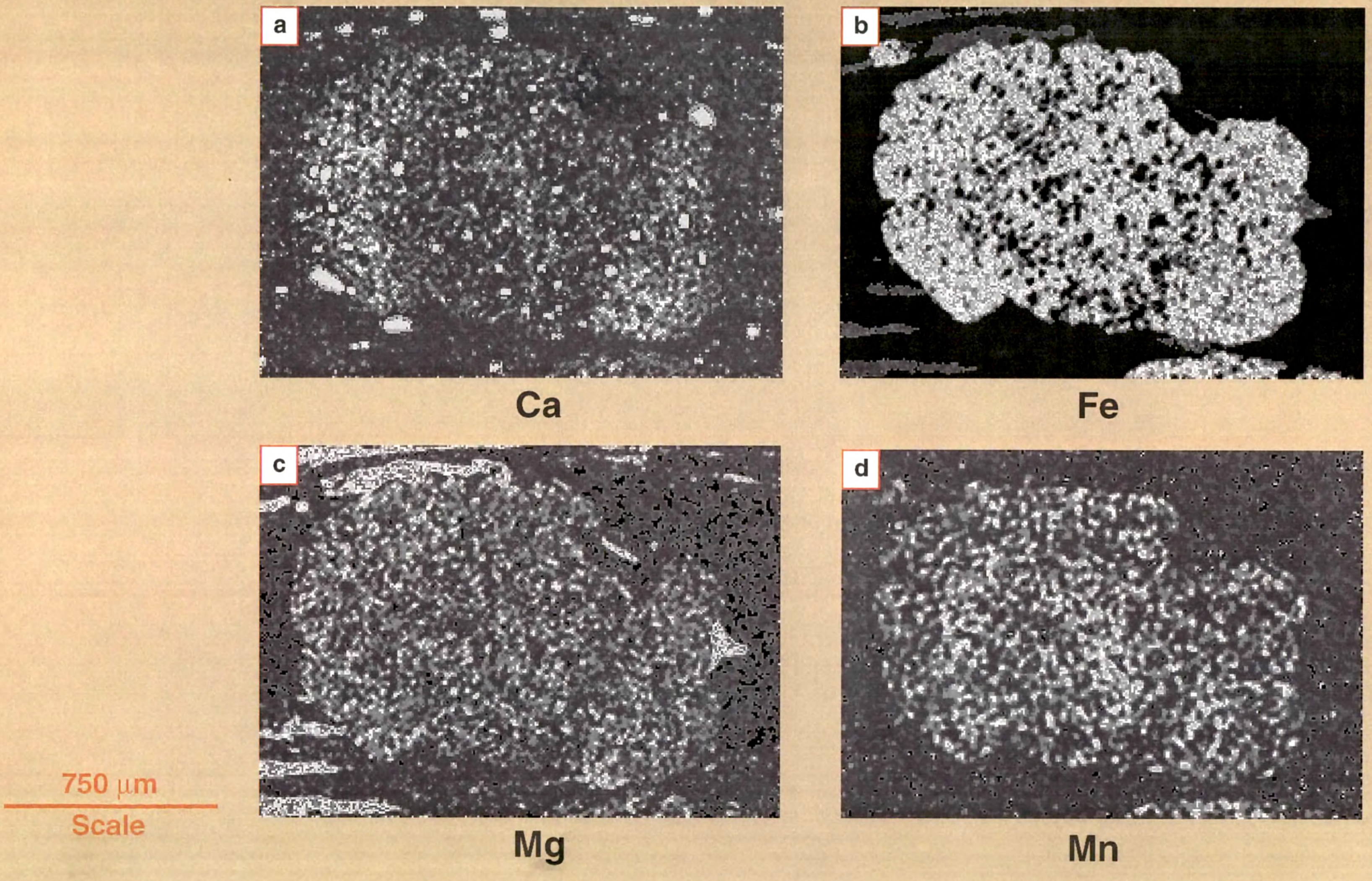

Fig. 7.5 . X-ray maps for (a) Ca, (b) Fe, (c) Mg and (d) Mn in garnet from Lunavada sample.

7.3. GEOTHERMOBAROMETRY

The data obtained from garnet, biotite, plagioclase, muscovite and ilmenite using the microprobe were subjected to thermobarometric calculations to understand the P-T conditions during the metamorphism. Thermobarometric calculations were made using the software *GTB of Kohn and Spear, version 1.9.* The following geothermometers and barometers were used:

Geothermometers :

Garnet-biotite (Ferry and Spear, 1978)

Geobarometers :

1. Garnet-plagioclase-biotite (Hoisch, 1990)
2. Garnet-plagioclase-biotite-muscovite (Hoisch, 1990)
3. Garnet-rutile-ilmenite-plagioclase-quartz; GRIPS (Bohlen and Liotta, 1986)

7.3.1. Thermobarometry of the Anjavana sample

Thermometric calculations for the core of the garnets were made using the composition of the core of the garnet porphyroblasts (syn-D_2) and core of biotite porphyroblasts (syn-D_2) in the matrix not in contact with garnet. Barometric calculations for the core were made using the composition of the core of garnet (syn-D_2), core of biotite (syn-D_2) not in contact with garnet, plagioclase in the matrix, muscovite in the matrix and ilmenite inclusions within garnet porphyroblasts. Temperatures for the rim were calculated using the composition of garnet rim (syn-D_2) and composition of biotite (syn-D_2) in contact with the garnet rim. Calculations for determining pressures for the rim were made using the garnet (syn-D_2) rim composition, biotite composition (syn-D_2) in contact with the garnet rim, composition of the matrix plagioclase, muscovite and ilmenite.

(a) Assumptions involved :

In an ideal situation, biotite inclusions within garnet should be used to carry out thermometric calculations for the garnet core. However, in the absence of biotite inclusions within garnet, it was assumed that the core of biotite porphyroblasts in the matrix grew in equilibrium with the core of garnet porphyroblasts (Spear, 1993). Plagioclase inclusions within garnet could not be detected; as a result, the composition of the matrix plagioclase was used to calculate the core pressures. It is important to mention here that considerable caution has to be exercised in interpreting P-T estimates obtained on the basis of such assumptions. Whilst the assumption made in order to calculate temperatures of the garnet core is easily justifiable on the basis of the similarity of size of the garnet and biotite porphyroblasts and the microstructural relationships, the assumptions made for calculating core pressures cannot be justified. As a result, the pressure calculations for the present sample are rather under-estimated and give only the apparent pressures. The entire exercise of carrying out thermobarometry on this sample was done to get a minimum estimate on the difference in the P-T conditions of the core and the rim of the garnets.

(b)Results :

The study revealed that the garnet core grew at 5kb and 420°C (apparent P-T conditions on the basis of the above assumptions) while the rim of the garnet grew at 4 kb and 490 °C (Fig. 7.6). This indicates that there was slight increase in temperature and an apparent decrease in pressure as the garnets grew. In other words there was probably a decompression along with thermal relaxation. It is once again highlighted here that the P estimates for the garnet core must be considerably greater than the apparent pressures of 5 kb

7.3.2. Thermobarometry of the Lunavada sample

Temperatures and pressures of the garnet core were calculated using the composition of the core of the garnet (syn-D_2) porphyroblasts and core of biotite (syn-D_2) porphyroblasts in the matrix not in contact with garnet. Barometric calculations for the core were made using the composition of the core of garnet (syn-D_2), core of biotite not in contact with garnet (syn-D_2), plagioclase in the core, muscovite in the matrix and ilmenite inclusions within garnet porphyroblasts. Temperatures for the rim were calculated using the composition of garnet rim (syn-D_2) and composition of biotite (syn-D_2) in contact with the garnet rim. Calculations for determining pressures for the rim were made using the garnet rim composition, biotite composition in contact with the garnet rim, composition of the matrix plagioclase, muscovite and ilmenite.

depleted?

(a) Results :

The thermobarometric calculations reveal that the core of the garnets formed at 13 kb and 600°C while the rim formed at 5.5 kb and 500°C (Fig. 7.7).

How will [illegible] 13 kb too high [illegible]

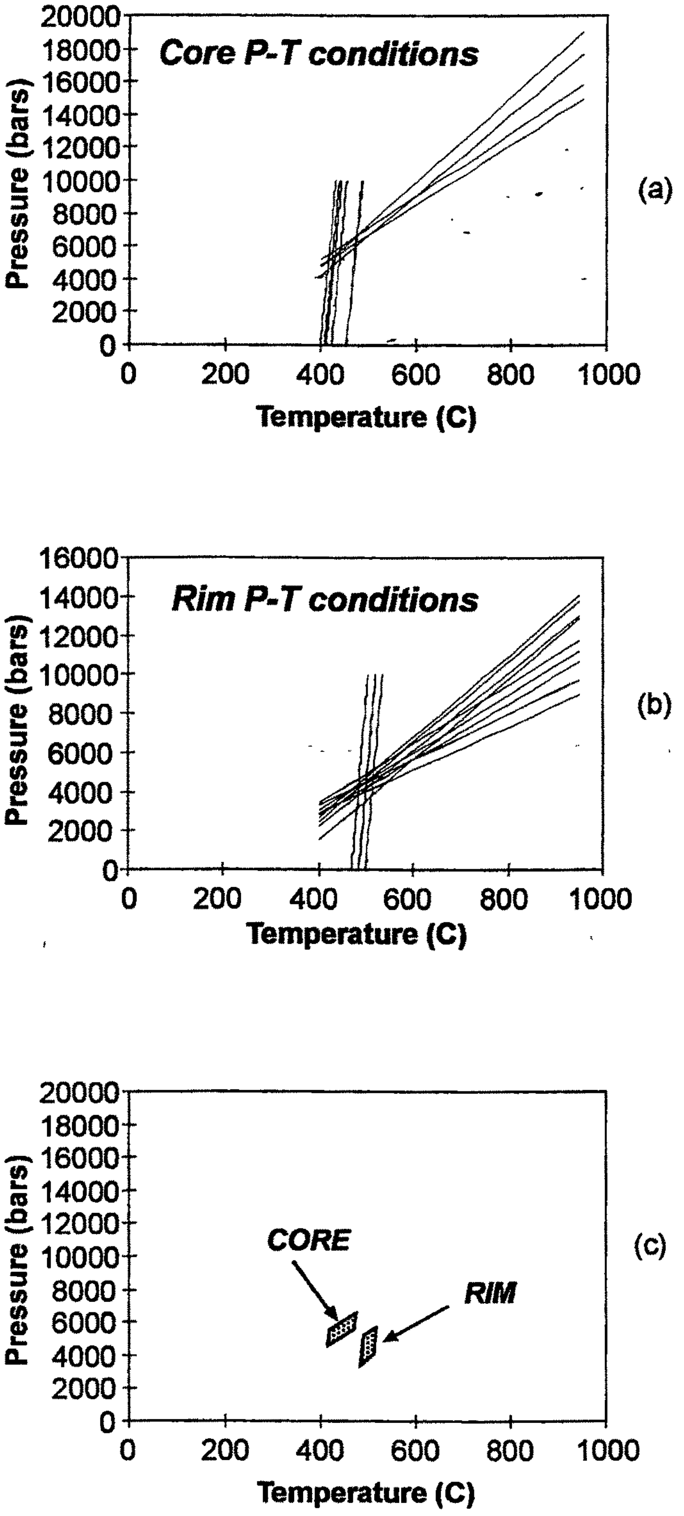

Fig.7.6. P-T conditions for garnet core (a) and rim (b) determined on the basis of thermobarometric calculations (Sample-Anjavana area). The P-T window for core and rim conditions obtained from figs. (a) and (b) are plotted together in (c) to highlight the variation in P-T conditions.

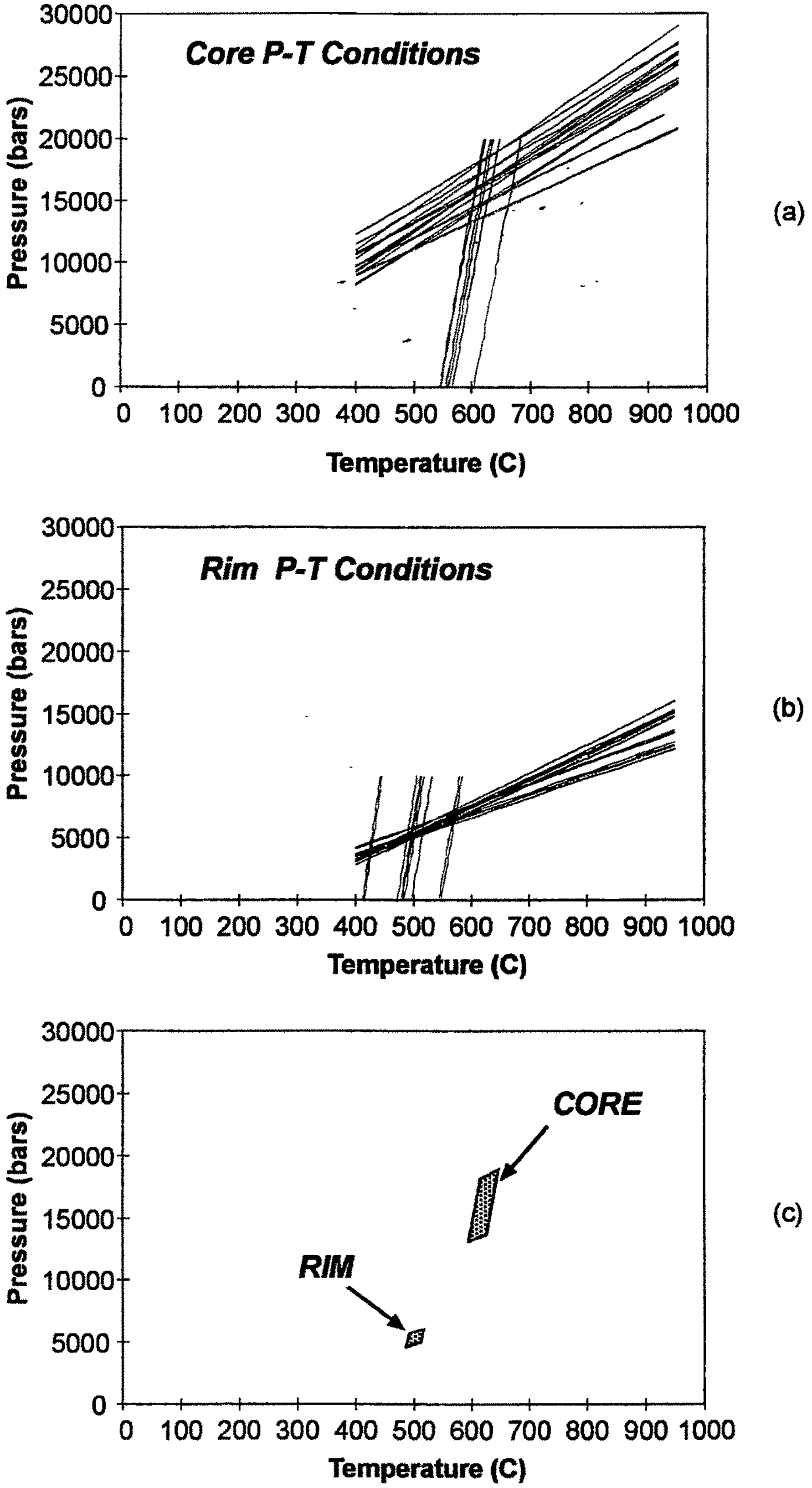

Fig.7.7. P-T conditions for garnet core (a) and rim (b) determined on the basis of thermobarometric calculations (Sample-Lunavada area). The P-T window for core and rim conditions obtained from figs. (a) and (b) are plotted together in (c) to highlight the variation in P-T conditions.

This indicates a release of pressure with a slight decrease in temperature during the growth of garnet from core to rim. However, in light of the indications of diffusion on the rim of this garnet (based on the garnet zoning profile, see section 7.2.2), caution has to be exercised to interpret the rim P-T conditions of this garnet. According to Spear (1993, p. 625), the temperatures calculated in such situations are lower than the actual temperatures at which the rim of the garnet grew. Therefore, it is quite logical to conclude that the garnet rim in the present case must have grown at temperatures greater than 500 °C.

7.3.3. Discussion

From the above description and data presentation it is clearly observed that there was a definitive release of P during garnet growth from the core to the rim which means that there has been considerable decompression during orogenesis of the Lunavada region. On the basis of the present data base, however, it is inadvisable to make any conclusions regarding change in temperatures during garnet growth. The Lunavada sample has given lower temperatures for the garnet rim composition as compared to the core. However, as discussed earlier (Section 7.2.2) the rim of the garnet has undergone diffusion and retrogression which resulted in lower T for the rim. On the other hand, thermobarometric calculations for the Anjavana sample gave a higher temperature for the garnet rim compared to the core of the garnet. This is indicative of an increase in temperature during garnet growth.

Pressures obtained for the garnet core in Anjavana sample are under-estimated because the core barometry for it was carried out using composition of matrix plagioclase. Since T is related to P and it is argued that there is a possibility of the garnet core of the Anjavana sample to have grown at temperatures higher than the calculated T. It has been mentioned in Section 7.3.1 that the actual P for the core of this sample must have been higher than the calculated P. This means that the T could have also been higher. From the thermobarometry on the Lunavada sample it is clear that the pressures for the core have been as high as 13 kb. Assuming 13kb to be the pressure at which the core of the garnet in the Anjavana sample grew and extrapolating the pressure data to 13[*] kb in Fig. 7.6a yields temperature of < 490 °C. The latter is the temperature at which the rim of the garnet in the Anjavana sample grew. Therefore, it is a possibility that the garnet core in the Anjavana sample formed at Pressures much higher than 5 kb.

The above comparative account of two samples belonging to the same orogen thus indicates that there was a definite decompression (release of pressure) with only slight change in temperature during the metamorphic history of Pre-Cambrian rocks of the Lunavada region. The fact that the temperatures did not change significantly during garnet growth is also supported by a linear Fe/Fe+Mg zoning profile for the Anjavana garnet. There was probably an isothermal decompression or decompression accompanied with a slight increase in temperature. During the cooling history, there was some retrogression which is revealed in the garnet zoning profile (Fig. 7.4) of the Lunavada sample.

(* Rutile could not be analyzed and the GRIPS barometer has been used for barometry. In the absence of rutile, the pressure is the highest possible pressure.)

7.4. FLUID INCLUSION STUDIES

A microscopic examination of doubly polished thick sections (≈ 100-200 μm) of garnet biotite schists revealed the presence of numerous fluid inclusions. Fluid inclusion studies can provide vital information about the fluids that were present during metamorphism, and thereby supplement the information on the thermal history of the rock, adding to the geothermobarometric studies carried out by other independent techniques (e.g. microprobe studies). With this in view, microthermometry was carried out on thick sections of garnet biotite schists from the Lunavada region. A detailed description of petrography and distribution of fluid inclusions is given here which is followed by a presentation of the results from microthermometric measurements and Raman micro-spectroscopy. It is important to mention here that only the fluid inclusions present in quartz crystals in the schist could be investigated in detail and hence the description in the present chapter pertains to inclusions in quartz. Although biotite, garnet and the quartz inclusions in garnet also show fluid inclusions, they were too small for microthermometric measurements.

7.4.1. Description of methods and techniques applied

Microthermometric measurements were made with the *Linkam Stage THM 600, England.* The stage was calibrated using synthetic fluid inclusions of pure H_2O and CO_2-H_2O mixtures for the melting temperatures of CO_2 at -56.6°C and of H_2O at 0°C and the chemical substance Phenanthrene ($C_{14}H_{10}$) which melts at 99.2°C (single grains of Phenanthrene were placed on the sample holder and subsequently only the grains that melt in the presence of a liquid rim reflect the true melting temperature). The sample was first subjected to rapid freezing experiments to measure the *temperature of nucleation* (T_n) of fluid inclusions. Freezing was achieved upto temperatures of -180°C. After having recorded the T_n for a particular inclusion, it was heated slowly upto room temperature (≈ 30°C) and the *temperature of melting* (T_m) and *temperature of homogenization* (T_h) of the carbonic fluid inclusions were recorded.

T_h of aqueous inclusions was not been measured; instead volume fraction estimates were made of the phases present at room temperatures. In some aqueous inclusions melting of clathrate phase (gas hydrate) was observed using the cycling method of heating and freezing on the Linkam stage. It must be kept in mind that heating experiments can often lead to decrepitation of the inclusions and loss of important information about the composition of the gases comprising the inclusions especially for high density carbonic fluid inclusions (the term "carbonic" is used for CO_2 rich mixtures with varying amounts of N_2 and CH_4). Based on this data and inclusion morphology, the inclusions were classified. From the clearly depressed melting temperatures of CO_2 rich inclusions which record the presence of other gases like N_2 and CH_4 it was found essential to carry out Raman analysis of a few inclusions.

Raman Spectroscopy is a useful non-destructive analytical method to determine the relative amounts of different gases present in a single fluid inclusion. The analysis was carried out at the *Free University, Amsterdam* with a *Dilor Microdil-28 multichannel laser Raman Microspectrometer* using a 514 nm Ar-ion laser as source of excitation. The instrument and the measurement conditions for fluid inclusions have been described by Burke and Lustenhouwer (1987) and by Burke (1994).

The data obtained from microthermometry and Raman microspectroscopy of the fluid inclusions was analyzed by using several computer programs developed by Dr. Ronald J. Bakker (personal communication; these programs are readily available at the University of Heidelberg, Germany). The following programs were used:

1. *HOMOGEN*: Calculation of densities and salinities of fluids.
2. *ISOCHOR*: This program traces isochores of inclusions in the P-T diagram.
3. *Q2*: Handling clathrate melting temperatures at Q2 conditions i.e. in the presence of four phases (clathrate, aqueous liquid, CO_2, liquid and vapour) (Bakker, 1997).
4. *NOSALT*: This program is also used to analyze clathrates in salt free systems (Bakker, 1997).

7.4.2. Petrography of thick section

The schist investigated showed the presence of garnet and biotite porphyroblasts. Fig. 7.8 is a schematic sketch of the thick section which was investigated for the present study. Garnet porphyroblasts have a size ranging from 0.4mm to 1.7mm and preserve the schistosity (S_1) in the form of quartz inclusion trails. In most garnets observed in the thin sections of this sample, the quartz inclusion trails lie at a high angle to the matrix foliation (S_2); the foliation (S_2) is constituted of biotite, muscovite and quartz and a few crystals of ilmenite.

The quartz crystals in the matrix show sharp extinction and preserve 120° triple points. Quartz crystals contain numerous fluid inclusions which were analyzed.

7.4.3. Microthermometry Data and Morphology of Fluid Inclusions

A petrographic study of the samples analyzed revealed the presence of fluid inclusions of varying size ranging from 15μm to <3μm diameter. They occur as isolated groups, along grain boundaries, cross-cutting inclusion trails and inclusion trails cutting across grain boundaries. Fig. 7.8 shows schematically the orientation and distribution of fluid inclusions.

The measurements revealed that the fluid inclusions could be classified into five types on the basis of petrography and microthermometric measurements.

Type-1:

The inclusions belonging to this category comprise large (15 to 4 μm diameter) generally equidimensional single phase inclusions (at room temperature) which occur as isolated clusters. Their shapes vary from spherical to cylindrical and some of them also show negative crystal shapes. Figs. 7.9, 7.10 and 7.11 show clusters of type-1 inclusions. From these figures it is clear that the inclusions of this type generally occur away from grain boundaries. Some of the inclusions of this type also have a daughter mineral (solid = Nahcolite determined from Raman analysis) within them. Inclusion "C" in Fig.7.11 is one such fluid inclusion with a solid within it. Figs. 7.12 and 7.13 are other examples of Type-1 fluid inclusions with a daughter mineral.

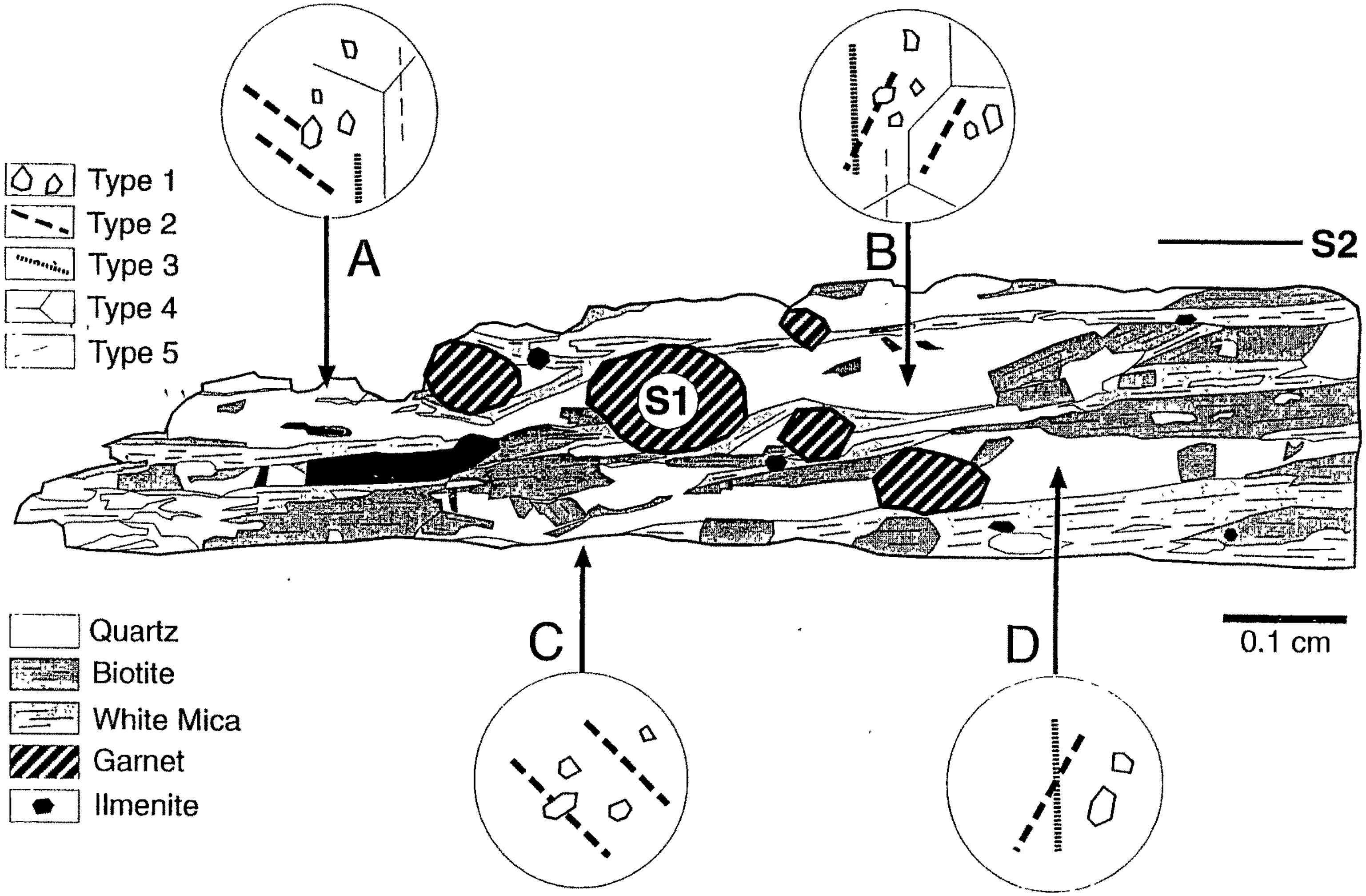

Fig.7.8. Sketch illustrating the occurrence of different types of fluid inclusions in the garnet biotite schists of the Lunavada region

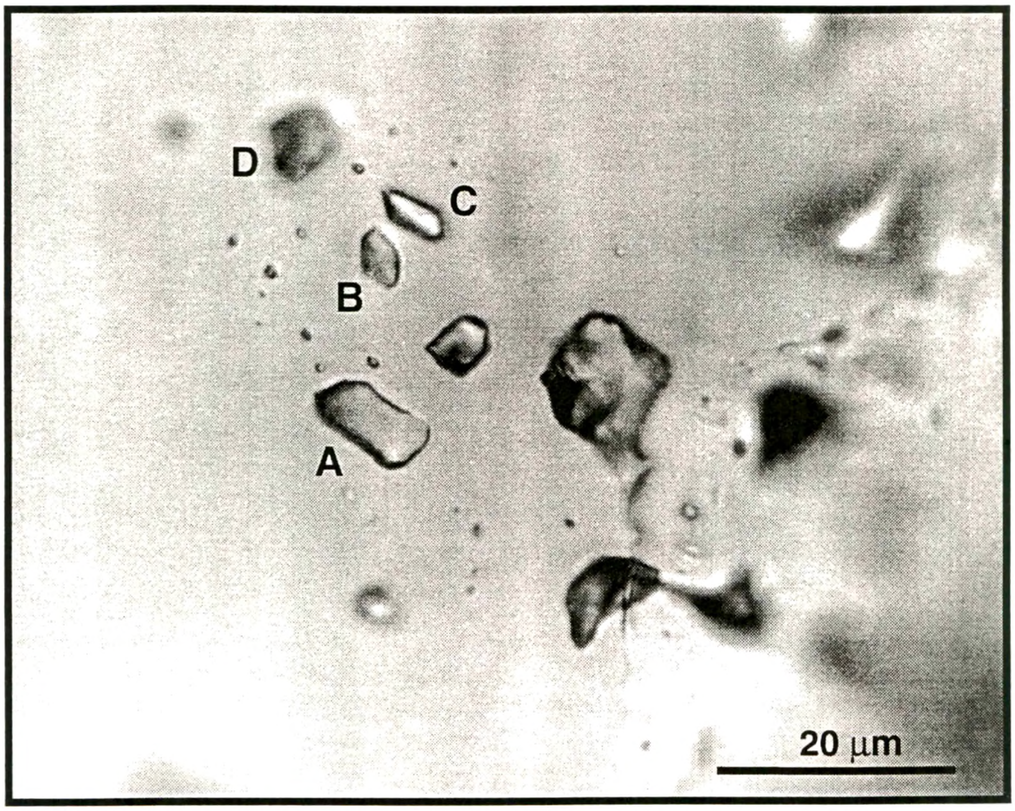

Fig. 7.9. Photomicrograph showing a cluster of Type-1 fluid inclusions in the mica schist studied. A, B, C and D are inclusion numbers 8a,b,c and d respectively in Table 7.3

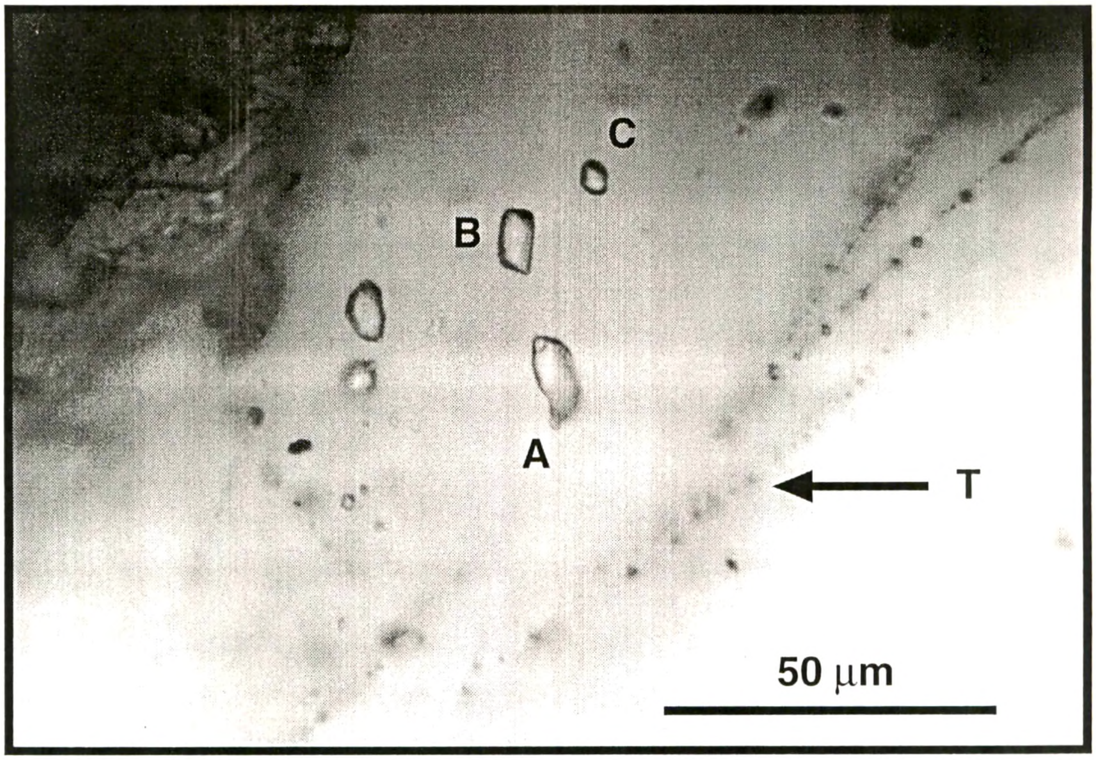

Fig. 7.10 Photomicrograph of a group of Type-1 fluid inclusions in quartz crystal of garnet biotite schist from Lunavada region. A, B and C are inclusion numbers M4, M2 and M3 respectively in table 7.3. T is a trail of secondary fluid inclusions.

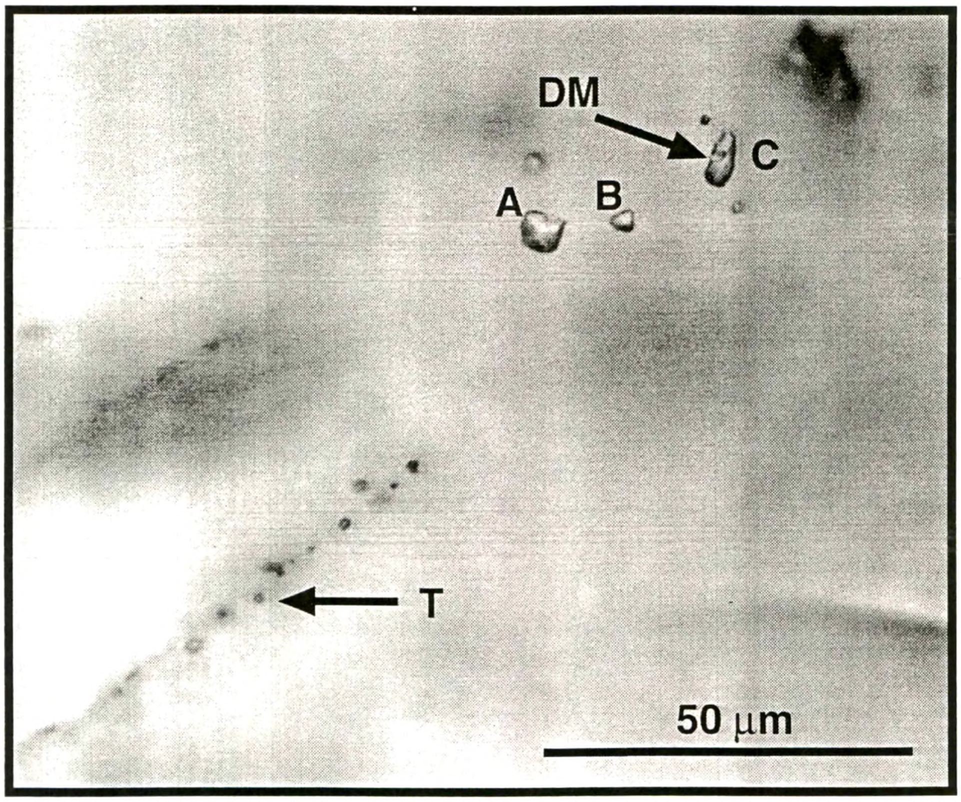

Fig. 7.11. Photomicrograph showing a cluster of Type-1 fluid inclusions in mica schist of Lunavada region. A, B and C are inclusion numbers 35, 36 and 37 respectively in table 7.3. Inclusion C has a daughter mineral (DM). T represents a trail of secondary inclusions.

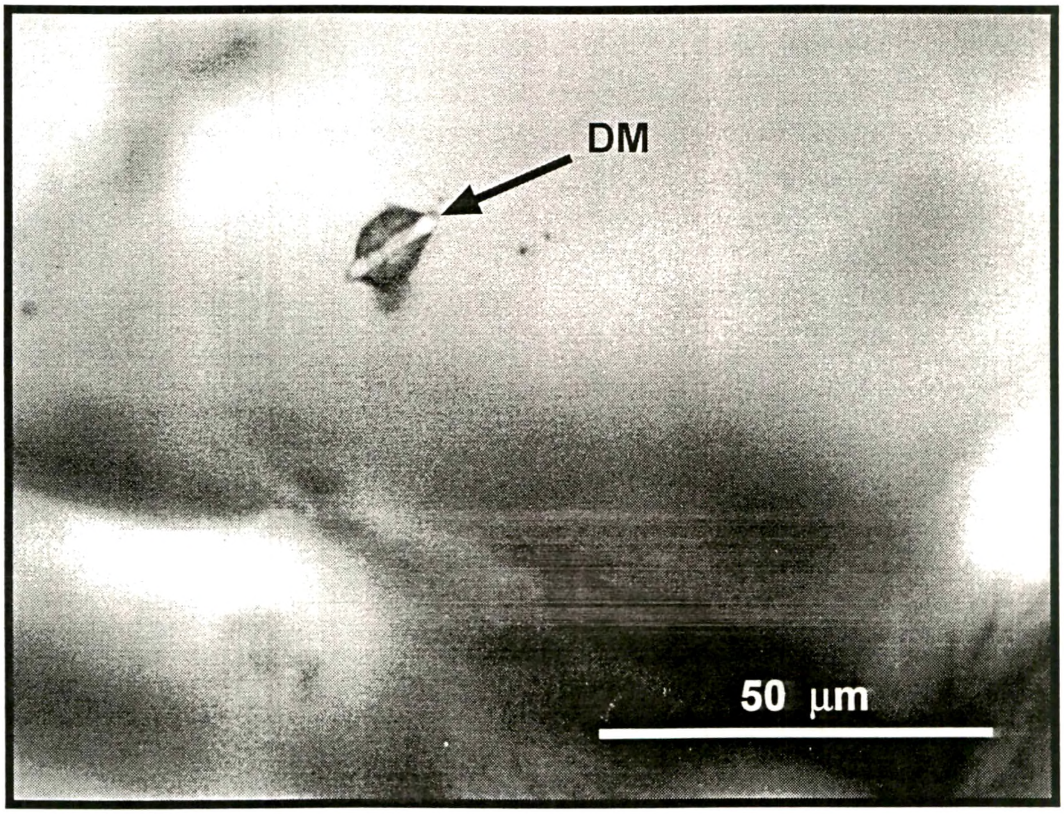

Fig. 7.12 Photomicrograph showing Type-1 fluid inclusion with a daughter mineral (DM).

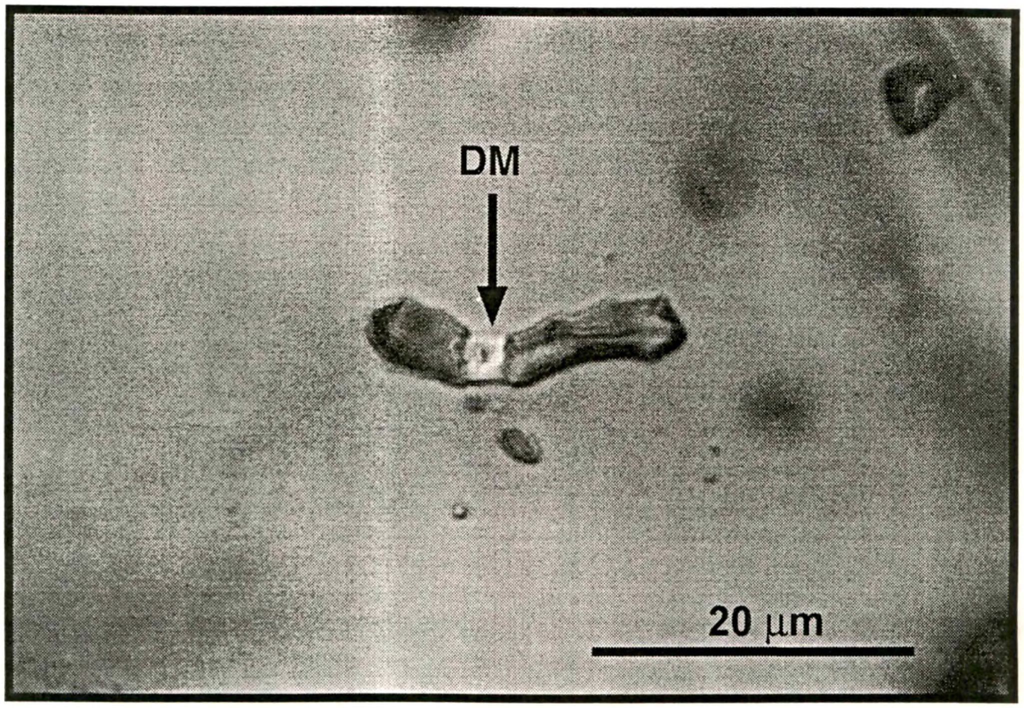

Fig. 7,13. Photomicrograph showing a Type-1 fluid inclusion with a daughter mineral (DM)

Microthermometric measurements have shown that the nucleation (T_n) of a solid phase occurs around -100 ^{0}C. Melting of this solid phase (T_m) ranges between -61^{0}C and -56^{0}C (Table 7.3). These inclusions have been interpreted as CO_2 rich fluids and the depression of the melting temperature of pure CO_2 implies the presence of other gases like N_2. Homogenization of the gas rich phases occurred generally into the liquid phase over a broad temperature interval between -36^{0}C and +22^{0}C. A few inclusions also homogenized in the vapour phase between -38.9^{0}C and 8.8^{0}C. This implies a relatively large range of densities for the Type-1 inclusions. Fig. 7.14 is the frequency diagram of the T_h of these CO_2 rich inclusions. It is clear from this figure that maximum number of type-1 inclusions homogenize between 0^{0}C and 20^{0}C while the other inclusions homogenize below 0^{0}C. To understand the relationship between the size of these inclusions and the T_h, the average diameter of each inclusion was recorded (Table 7.4). Fig. 7.15 is a graphical representation of the data presented in Table 7.4 and it clearly reveals that there is a systematic relation between the T_h and the average diameter of each inclusion. All the fluid inclusions having an average diameter >8µm have a T_h >7^{0}C whilst those inclusions which have a T_h below 0^{0}C are <8µm in diameter. This implies a direct relationship between the density of the fluid inclusions and their size. Smaller inclusions tend to have higher densities and lower T_h.

Table 7.3

Microthermometry data of Type-1 fluid inclusions. The symbol * has been used wherein the V_m was determined on the basis of actual CO_2% and N_2% from Raman microspectroscopy.

Inclusion Nr.	T_n	T_m (CO_2)	T_h (CO2)	Daughter	Morphology	Estimated V_m (cc/mole)	Estimated CO_2 (%)	Estimated N_2 (%)
7	-93	-57.1	20.3		negative crystal	*		
8a	-99.3	-56.9	20		rectangular	*		
8b	-99.3	-56.9	20		almost cylindrical			
8c	-99.3	-56.9	20		almost cylindrical			
8d	-99.3	-56.8	21.6		almost negative	60	97.5	2.5
16	-96.3	-55.1	15.8		spherical			
17	-96.1	-56.7	18.3		spherical	56	98	2
20	-100	-56.8	8.9		cylindrical	50	98	2
32	-101	-57.2	-23.7		cylindrical	*		
33	-101	-57.2	-34.2		cylindrical	*		
34	-101	-57.07	-18.03		almost spherical	44	97.5	2.5
35	-100.4	-57.1	-5.7		3-D amoeboid	*		
36	-101	-57.36	-5.66		almost spherical	47	96	4
37	-100.3	-57.1	-5.4	+	cylindrical	*		
R1-A3	-89.4	-57	3.4		cylindrical	49	97.5	2.5
R1-A.2	-89.4	-57	6.5		irregular	51	96.5	3.5
R1-A.1	-93.0		8.1		almost cylindrical			
R2	-93.0	-58.4	4.1		negative (hexagonal)	59	85	15
R3.1	-93.0	-57.7	12.3	+	cylindrical	60.5	91	9
R3.2			15.2		irregular			
R4.1		-57.3	5.0		spherical	52	95.5	4.5
R4.2	-91.2	-57.3	5.6	+	irregular	52	95.5	4.5

R4.3			-2.3		almost spherical			
R4.4		-56.9	-1.7		almost cylindrical	48.5	98.5	1.5
R5.1	-91 2	-56.8	-2.8		spherical	47	99	1
R5.2	-89.4	-56.7	0.9		irregular	48.5	99	1
R5.3	-93.0	-57.6	1.0		negative (hexagonal)	50.7	93.8	6.2
R6.1	-93.0	-58.2	4.6		negative (hexagonal)	55	89	11
R6.2	-92.1	-57.7	0.3		almost cylindrical	50.5	93.5	6.5
R6.3	-93.0	-57.7	7		irregular	55.5	92	8
R7	-93.0	-56.6		+	irregular			
R11.1	-92.1	-57	-0.9			47.5	98	2
R13	-100.9	-61.2	18.2		almost spherical			
R14	-98.1	-58.5	-23.4		irregular	45	89	11
R18		-58.9	-9.1(liq)		almost spherical	51.5	84	16
R20.2			-23.4	+	irregular			
R21		-57.9			irregular	50.3	92	8
R22	-98.1	-59.3	-16.2		irregular	50.5	98	2
R23		-59.4	-15		irregular	51.5	97.7	2.3
R24	-97.1	-58.2	-0.3		irregular	50.5	90.5	9.5
R25		-58.9	-10.2		irregular	50.3	84	16
R26		-59.1	-15		irregular	49	83	17
R27	-95.2	-57.5	12.5		cylindrical	57	94	6
R28		-57.7	13.8	+	cylindrical	64	91	9
R29					rectangular			
R33		-57.2	-1.9		irregular	48	96.5	3.5
R34		-57.7	-6.2		irregular	48.5	93	7
R35		-57.6	0 3		almost spherical	50	94	6
R36		-57.9	-22.4		irregular	44	93	7
R37 =32	-95.2	-57.6	-24.3		cylindrical	43	95	5
R38= 33	-97.1	-57.7	-35.4		cylindrical	41.5	94	6

R39= 34	-95 2	-57.6	-12		irregular	46	94	6
R40= 37	-95.2	-57.5	-5.4	+	cylindrical	47.5	95	5
R41= 36	-97.1	-57.9	-6.2		irregular	48.5	93	7
R42		-57.4	-3.2		irregular	48	95.5	4.5
R43= 35	-96 2	-57.6	-6.7	+	irregular	48	94.5	5.5
R44					irregular			
R45		-59.3	8.1	+	almost cylindrical	*		
R46			15		irregular			
R47	-94.3	-57.6	17.3	+	irregular	70	90.5	9.5
R48		-57.7	14.7		almost cylindrical	64	91	9
R49		-58.3	7.6		irregular	62	86	14
R50		-58.3	2.0	+	cylindrical	55.3	87	13
R51		-58.2	2.0		irregular	54	89	11
R52	-100.2	-59.4	6.3		irregular	*		
R53.1			9.5		irregular			
R53.2			10.4		almost cylindrical			
R54.1		-58.9	10.6		irregular	*		
R54.2		-58.5	10.5		irregular	*		
R55		-60.1(?)	3 6		irregular	*		
R56		-58.1	17.3		cylindrical	*		
R57	-97.3	-58.0			negative (hexagonal)			
R57x		-61.4	13.1		cylindrical	*		
R60	-95.2	-56.3			negative (hexagonal)			
R61	-95.2				irregular			
M1	-105	-58.6			almost spherical			
M2	-102	-58.1	19.4		cylindrical	60	95	5
M3	-102	-58.1	19.4	+	almost cylindrical	60	95	5
M4	-98	-55.7	19.4		spherical			
M5	-103	-58.0	17.4		spherical	58.5	95	5

M6	-103	-58.1	15.4		spherical	58	95	5
M7	-103	-58.1	15.4		almost spherical	58	95	5
M8	-100	-56.6	14.1		almost spherical			
M9	-101	-57.6	15.4		almost cylindrical	56.5	97	3
M10	-101.5	-58.0			cylindrical			
R71.1		-56.2	6.5		almost cylindrical			
R74		-57	12.3	+	cylindrical	54	99	1
R75		-56.2	-1.3		cylindrical			
R76		-57.2	-1.8		cylindrical	47	99	1
R77		-57.7	5.9		cylindrical	56	97	3
R78		-57.7	5.4		cylindrical			
R84		-57.3		+	cylindrical			
R88		-57.2	4.4	+	cylindrical	50	98	2
R89		-56.4	-0.8		cylindrical			
R90		-56.9	1.1		almost cylindrical	52	100	
R91		-57.4	4.8	+	spherical	50	99	1
R92		-57	7.0	+	almost cylindrical	55	99	1
R94		-57	0.4		almost spherical	52	99	1
R95		-56.2	-2.6		spherical			
R96		-57.7	4.3		cylindrical	50	95	5
R15		-58.6	-29.2 (vap)		irregular			
R16		-58.4	-21.9 (vap)		irregular			
R17		-59.6	-38.9 (vap)		irregular			
R19	-99	-60	-14.9(vap)		almost cylindrical			
R20.1		-59.6	-16.6 (vap)		irregular			
R86		-57.4	8.8 (vap)		almost cylindrical			

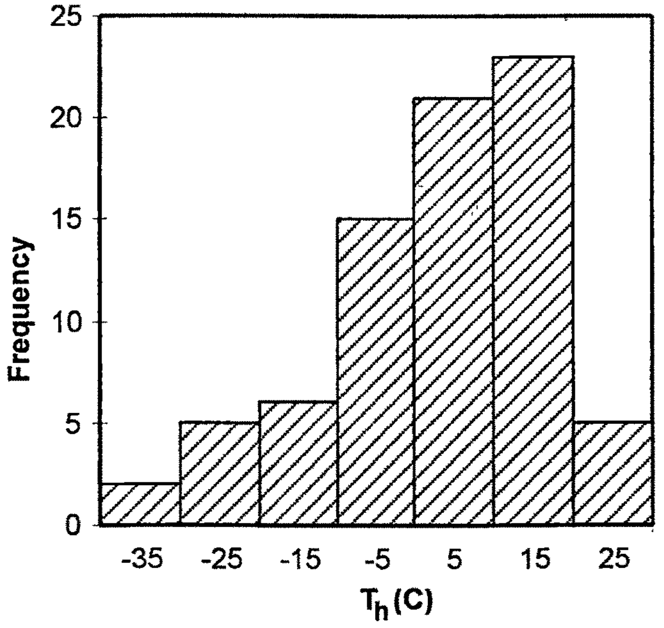

Fig. 7.14. Frequency diagram for Type-1 fluid inclusions (homogenizing in the liquid phase)

Table 7.4

Data of homogenization temperatures of Type-1 CO_2 inclusions (homogenizing in the liquid phase) and the average diameter. The average diameter for an inclusion is the average of the longest and shortest dimensions.

Inclusion Nr.	Average Diameter (μm)	Th (CO_2)
7	11.5	20.3
8a	7.4	20
8b	4.4	20
8c	4	20
8d	6.4	21.6
16	4.4	15.8
17	6.1	18.3
20	3.7	8.9
32	3.7	-23.7
33	4	-34.2
34	3	-18
35	5.7	-5.7
36	2.7	-5.66
37	5.4	-5.4
R1-A3	5.1	3.4
R1-A.2	4.7	6.5
R1-A.1	3	8.1
R2	2	4.1
R3.1	4.4	12.3
R3.2	3	15.2
R4.1	2.7	5
R4.2	5.1	5.6
R4.3	3.4	-2.3
R4.4	4.4	-1.7
R5.1	5.4	-2.8
R5.2	4.4	0.9
R5.3	5.7	1
R6.1	4.7	4.6
R6.2	6.1	0.3
R6.3	4	7
R11.1	3.7	-0.9
R13	4.7	18.2
R14	5.7	-23.4
R18	4.4	-9.1
R20.2	4	-23.4
R22	5.7	-16.2
R23	4.7	-15
R24	4.7	-0.3
R25	4	-10.2
R26	4	-15
R27	4.7	12.5

R28	3	13.8
R33	5.1	-1.9
R34	6.7	-6.2
R35	4.4	0.3
R36	4	-22.4
R42	3	-3.2
R45	9.1	8.1
R46	5.4	15
R47	14.2	17.3
R48	3.4	14.7
R49	4.7	7.6
R50	5.4	2
R51	6.4	2
R52	5.1	6.3
R53.1	4.1	9.5
R53.2	4	10.4
R54.1	4.4	10.6
R54.2	6.1	10.5
R55	6.1	3.6
R56	3.7	17.3
R57x	4.7	13.1
M2	7.4	19.4
M3	4.7	19.4
M4	9.5	19.4
M5	6.1	17.4
M6	2.7	15.4
M7	2.7	15.4
M9	8.8	15.4
R71.1	4.4	6.5
R74	4.4	12.3
R75	4.4	-1.3
R76	3.4	-1.8
R77	5.1	5.9
R88	3.4	4.4
R89	3.7	-0.8
R90	5.7	1.1
R91	4.4	4.8
R92	4.4	7
R94	4.4	0.4
R95	6	-2.6
R96	5.1	4.3

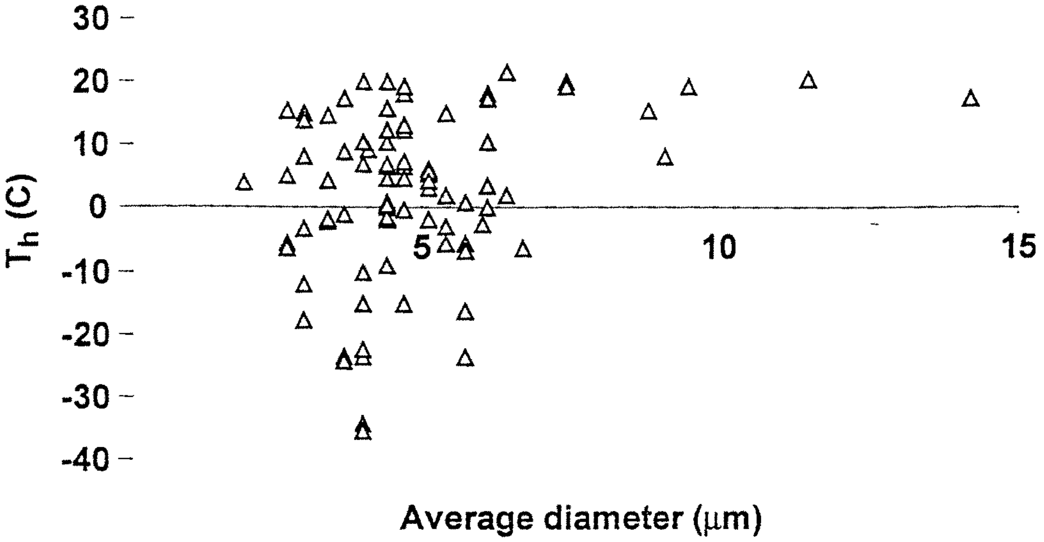

Fig. 7.15. Graph of average diameter of Type-1 fluid inclusions (homogenizing in the liquid phase) against T_h

Type-2:

The inclusions belonging to this type are morphologically regular shaped and of small size, in general rather too small (<1μm in diameter) for microthermometrical analysis. They dominantly comprise two phases - liquid and gas at room T. They occur along inclined inclusion trails manifesting healed cracks which lie oblique to the S_2 schistosity. Fig. 7.16 is a schematic drawing illustrating type-2 inclusions along inclined trails. The S_2 schistosity is parallel to the long axis of the figure and the fluid inclusion trail lies oblique to the S_2 as well as to the field of view. A few of these inclusion trails lie oblique to each other, which in all probability represent conjugate sets. Occasionally, these trails include clusters of larger fluid inclusions (upto 15μm in diameter) which consist of a mixture of two types of fluids (Figs. 7.17, 7.18 and 7.19). Aqueous inclusions show a filling degree of about 80-90 vol% and a few also show a moving gas bubble (inclusion A in Fig. 7.18). Such inclusions have a regular shape usually like a cube. These occur together with bigger and more irregular shaped inclusions which show a lower degree of filling (around 10%) (e.g. inclusion B in Fig. 7.18). A few large fluid inclusions clearly show a rim of H_2O (inclusion B in Fig. 7.19). These inclusions are party recycled type-1 inclusions which occur along these trails of type-2 inclusions. They tend to have a very low density carbonic vapour phase and sometimes a small rim of H_2O. Such fluid inclusions did not show any change during microthermometry and no measurements could be made on them.

Microthermometric measurements reveal that these inclusions comprise mixed fluids. Melting temperatures of CO_2, gas hydrate (clathrates) and ice

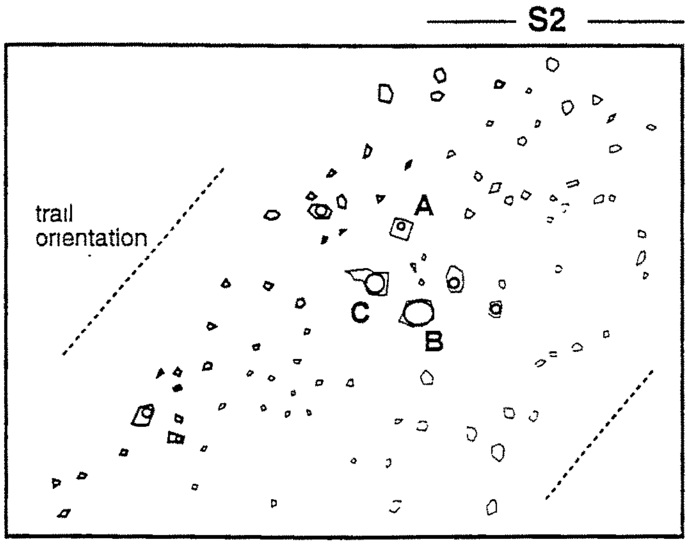

Fig. 7.16. Schematic diagram illustrating the occurrence of Type-2 fluid inclusions in quartz crystals of mica schists of Lunavada region. A, B, and C simulate inclusion numbers 26, R.69 and 27 repectively in Table 7.5

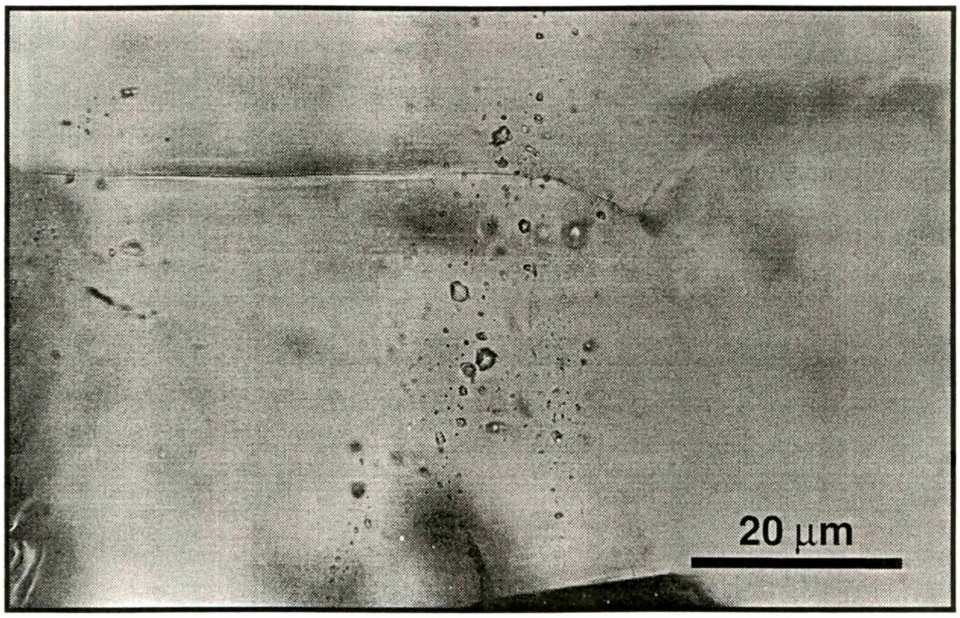

Fig. 7.17. Photomicrograph documenting the occurrence of Type-2 fluid inclusions along inclusion trails.

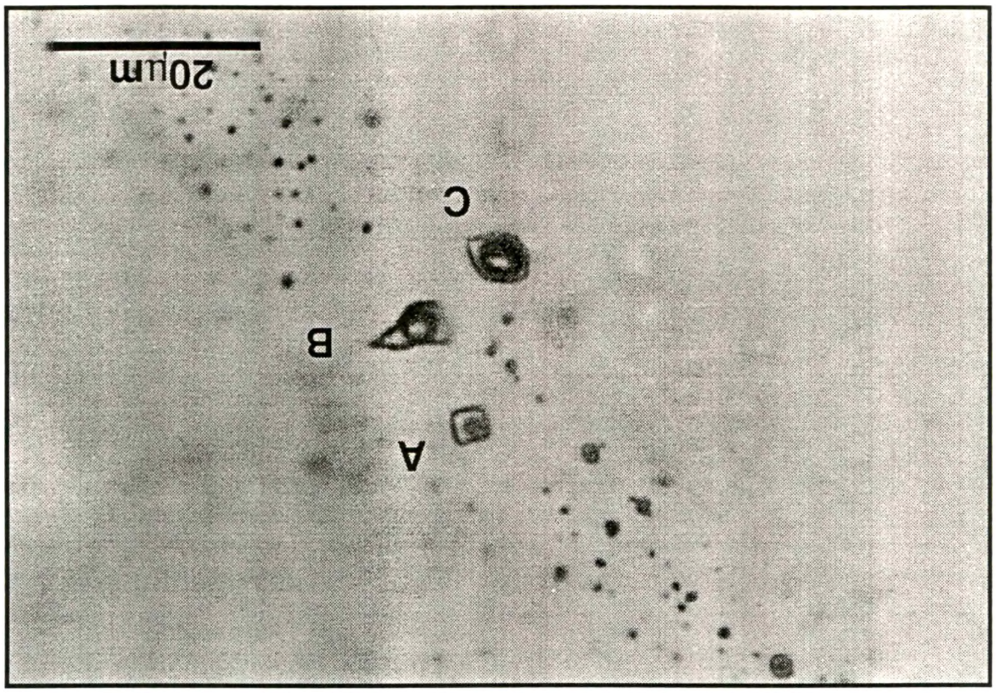

Fig. 7.18. Photomicrograph of inclusion trails with Type-2 fluid inclusions. A, B and C are inclusion numbers 26, 27 and R60 in table 7.5

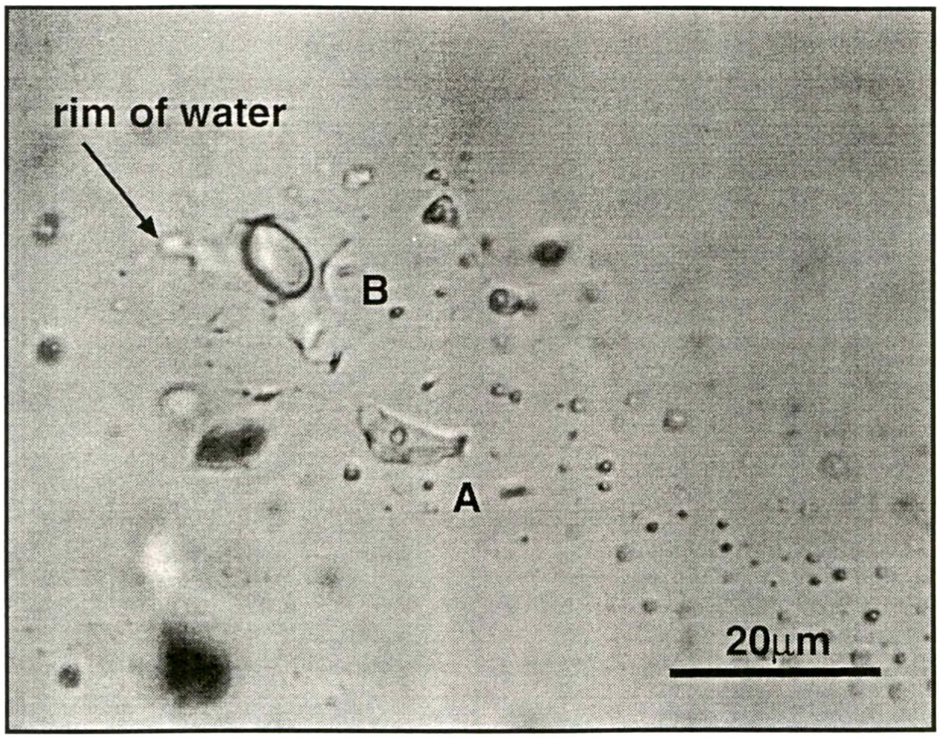

Fig. 7.19. Photomicrograph documenting presence of aqueous fluid inclusions (Type-2) along trails. A and B represent inclusion numbers 30 and 31 in Table 7.5

Table 7.5

Microthermometry data of Type-2 fluid inclusions. Values with the superscript * were determined through Raman microspectroscopy.

Incl.Nr	T_n	T_e	T_m (Clth)	T_m (CO_2)	T_h (CO2)	T_m (aq)	Vol% (gas)	Morphology	V_m (cc/mole)	wt% NaCl	CO_2 (%)	H_2O (%)	CH_4 (%)
12	-45.3					-2.3	1	cylindrical	18.23	3.867			
15	-53.2	-7.6				-5.6	5	cylindrical	19.00	8.680			
24	-53.4					-4.6	7	almost spherical	19.41	7.307			
26	-47.5	-25 to -20				-3.8	7	regular square	19.41	6.156			
30	-49.3					-5.8	1	irregular	18.23	8.946			
R8.3						-4.9	20	cylindrical	22.560	7.726			
R31	-44.7					-4.2	10	almost cylindrical	20.05	6.737			
R62	-49.5					-5.3	10	almost spherical	20.05	8.275			
R63						-2.8	40	almost spherical	30.08	4.65			
R64						-3.8	20	almost spherical	22.560	6.156			
R65						-6.1	20	cylindrical	22.560	9.34			
R93	-49.5					-3.0		cylindrical					
14	-50.3	-21.2	7.6				2	cylindrical	19.01		2.6	97.4	
21	-30.9		8.7				30	almost cylindrical	26.22		4.5	95.5	
22	-31.1		8.7				30	almost cylindrical	26.22		4.5	95.5	
23	-31.5		7.8				30	almost spherical	26.25		4	96	
25	-32.1		7.8				30	almost cylindrical	26.25		4	96	
27	-36.7		6.8				40	irregular			50 *		50 *
28	-38.9		8.8				30	almost spherical	26.21		4.6	95.4	
29	-30.6		8.7				50	cylindrical	35.86		6.7	93.3	

31	-29.7		9.8				40	irregular			86 *		14 *
R12			7.4				60	cylindrical	44.45		7	93	
M13	-35.8		10.2				40	almost cylindrical					
M14	-39		7.3				20	almost spherical	23.11		3.3	96.7	
M15	-37.5		8.4				20	almost spherical	23.11		3.7	96.3	
M16			7.4				40	almost spherical	30.41		4.6	93.4	
M17	-37.5		8.0				30	almost spherical	26.25		4.1	93.9	
M18	-36.5		9.2				30	almost spherical	26.18		4.8	95.2	
R21.1			4.2				7	cylindrical	19.92		2.2	97.8	
R97			13.5					almost spherical					
R8.1	-93			-57.1	14.6 (vap)		80	cylindrical	73.066		23.0		
R8 2	-93			-56.7	12.7 (vap)		90	almost cylindrical	118.54		37.5		
R13	T_n CO_2 = -100.9 and T_n (Clth) = -34		5.5	-61.2	18.2		30	spherical	23.45				
R21.2			0.2	-57.9			15	cylindrical	21.69		1.7	98 3	
R60	T_n (CO_2) = -95.2		7.6	-56.3			80	negative hexagonal	82.23		1.4	98.6	

(aqueous phase) could be measured. Table 7.5 shows the entire data set recorded for such inclusions. For those inclusions whose homogenization of the carbonic phase could be measured, only low to very low densities could be inferred for such vapour like fluids. In a few inclusions the melting temperatures of CO_2 as well as the aqueous phase could be recorded while in others the melting temperatures of the gas hydrates as well as CO_2 could be recorded. Such inclusions can be considered to form the first end member of this group. The second end member comprises fluid inclusions which give only the T_m of the aqueous phase. Inclusions consisting of only the gas hydrates comprise the intermediate type. The heating experiments on these inclusions show that the T_h (liquid) is around +400°C.

Type-3:

Similar to type-2 inclusions, these also constitutes small (generally <2μm; sometimes bigger) equidimensional two phase aqueous fluid inclusions associated with big (around 13μm) dark three dimensional single phase inclusions, the latter of which do not show any response on freezing upto -165°C during microthermometry. The inclusions reveal only one pronounced orientation and lie almost perpendicular to the S_2 schistosity and therefore also at an angle to trails of type-2 fluid inclusions.

The two-phase aqueous fluid inclusions record very low melting temperatures for ice ranging between -9.3°C and -30°C implying high salinities. Very low eutectic temperatures (< -40°C) were recorded for a few inclusions which is an indication of the presence of $CaCl_2$ salt. Table 7.6 shows the entire

Type 7.6

Microthermometry data of Type-3 fluid inclusions.

Incl.Nr	**T_n (°C)**	**T_e (°C)**	**T_m (aq) (°C)**	**T_h (°C)**	**Vol% (gas)**	**Morphology**	**V_m (cc/mole)**	**Salinity (wt%$CaCl_2$)**
3	-58	-50.3	-14		5	almost cylindrical	19.0	17.28
9	-70.6		-20.7		5	almost cylindrical	19.0	21.53
11	-57.4		-19.8		20	almost cylindrical	22.56	21.02
13	-68.6		-23.4		10	almost cylindrical	20.05	22.96
M11			-19.8			spherical	19.41	21.02
R79				-154 (vap)	70	cylindrical		
R79.1			-9.3		25	cylindrical	24.06	13.42
R80	-78.2		-18.4		1.5	spherical	18.32	20.19
R81	-76.3		-18.8		20	almost cylindrical	22.56	20.44
R98	-53.3	-46.6 to -44.7	-17.2		10	almost cylindrical	20.05	19.46

data set recorded from microthermometry of type-3 inclusions. Moreover, there are also a few two phase aqueous inclusions belonging to this category which did not show any changes during microthermometry (e.g. Fig. 7.20).

It is envisaged that the dark big fluid inclusions might be representing pre-existing primary inclusions which opened during fracturing or cracking and subsequently got refilled by later fluids. They are in general very dark, possibly indicate a coating of a thin layer of graphite on the inclusion walls. Only in one inclusion a homogenization temperature of -154°C in the vapour phase could be measured (Table 7.6); this illustrates that the carbonic phase must be rich in either CH_4 or N_2. On the basis of these evidences it is concluded that the type-3 inclusions constitutes very low density carbonic fluid inclusions in association with aqueous fluid inclusions.

Type-4:

To this type belong the inclusions occurring along grain boundaries and sub-grain boundaries of the quartz crystals (Fig. 7.21). They are irregular shaped inclusions and have a size of 1-2µm. Some of them are worm shaped, irregular voids and dendritic channels which are typical of grain boundaries. No microthermometry could be carried out on these inclusions on account of their small size.

Type-5:

These comprise highly irregular and flat H_2O rich fluid inclusions. They occur along straight flat lying trails which sometimes cut through grain

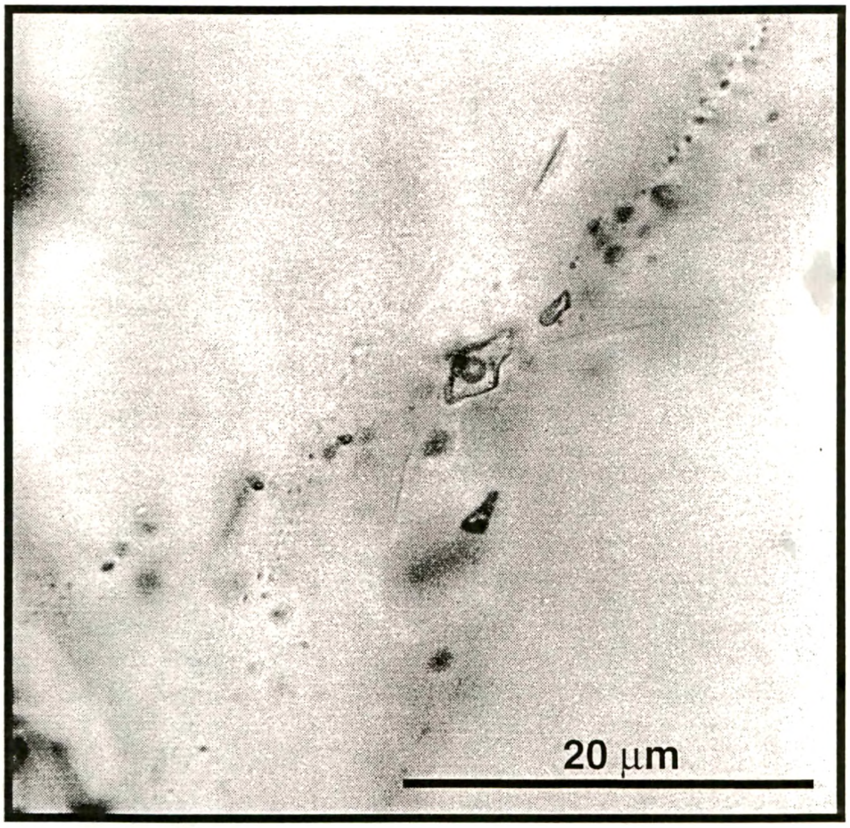

Fig. 7.20 Type-3 fluid inclusions along a trail in quartz crystal from garnet biotite schist of the Lunavada region

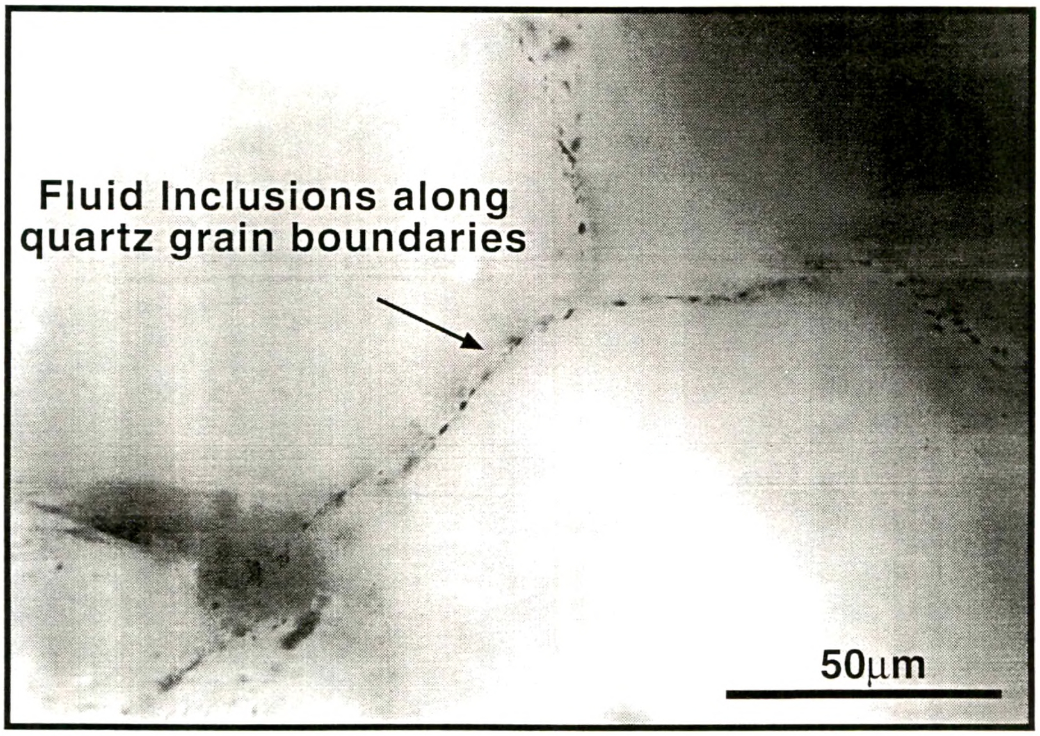

Fig. 7.21. Type-4 fluid inclusions along quartz grain boundaries.

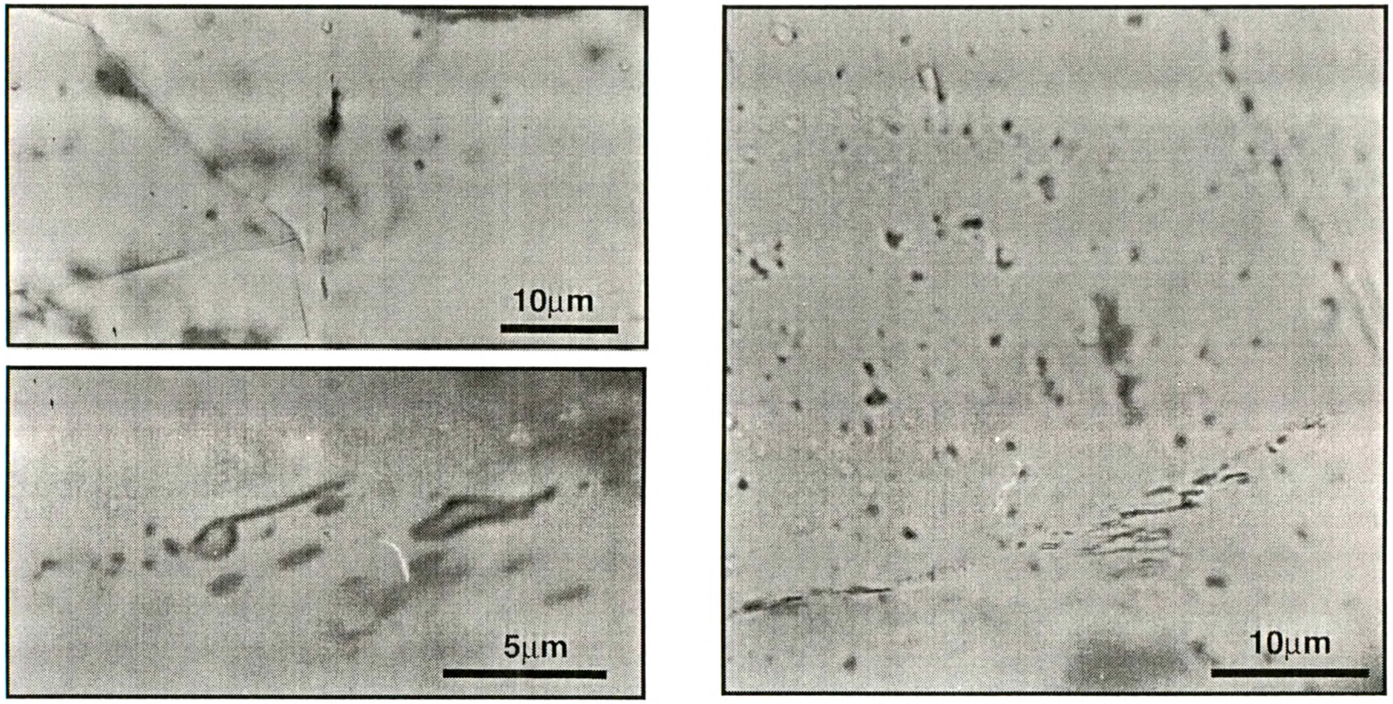

Fig. 7.22. Photomicrographs of Type-5 fluid inclusions in quartz crystal occurring in garnet biotite schist from Lunavada region

boundaries of quartz crystals (Fig. 7.22). These clearly belong to the last generation of fluid inclusions observed in the sample and have a very high degree of filling (> 80 %). T_m of the ice of around -0.3°C in one inclusion indicates the presence of minor amounts of salts.

7.4.5. Raman Analysis

A total of 12 inclusions were analyzed with the Raman microspectrometer for a qualitative and relative quantitative analysis of the carbonic phase. It was found that the fluid inclusions posses varying percentages of CO_2, N_2, and CH_4. Figs. 7.23 a,b,c show characteristic Raman spectra obtained for some of the analyzed fluid inclusions. CO_2, N_2 and CH_4 show characteristic peaks for the vibration modes of these molecules at 1388 cm^{-1} & 1286 for CO_2 (also referred to as the CO_2 Fermi doublet peaks, Burke and Lustenhouwer, 1987), 2331 cm^{-1} for N_2 and 2917 cm^{-1} for CH_4.

Type-1 inclusions have > mole% CO_2 and the remaining gas species is N_2 (high density CO_2 ; Table 7.7). Raman analysis of the larger dark inclusions belonging to type-2 reveals the presence of varying percentages of CH_4 along with CO_2 and total absence of N_2 (aqueous in Table 7.7). A few big type-3 fluid inclusions show varying amounts of CO_2, CH_4 and N_2 (low density carbonic in table 7.7). Some of these show the presence of CO_2 with either CH_4 and N_2 whilst others consist only of CH_4 and N_2 with total absence of CO_2.

On the basis of the results from microthermometry and the gas percentages determined from Raman analysis, the molar volume (Table 7.7) of

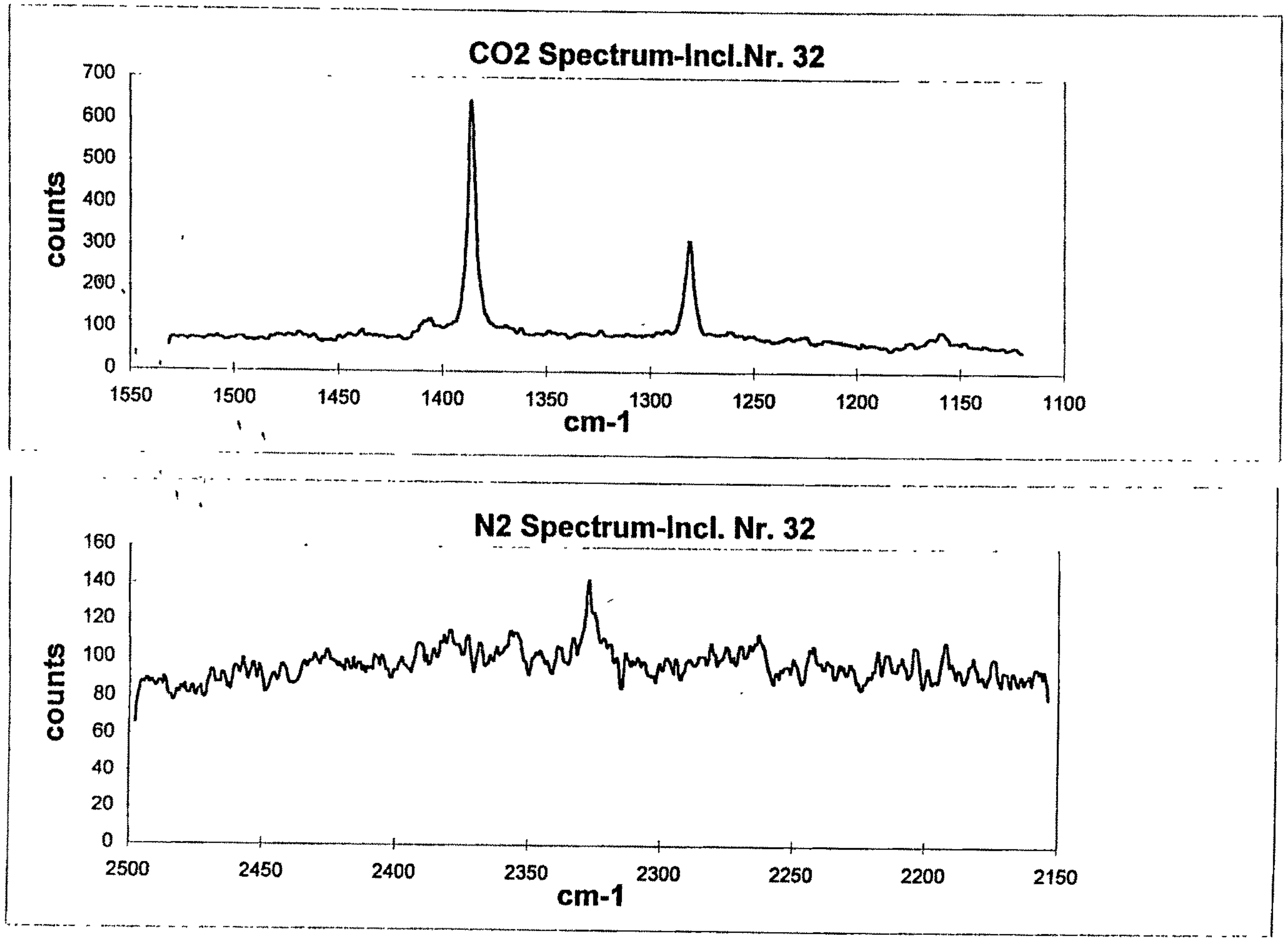

Fig. 7.23a, b (Caption on following page)

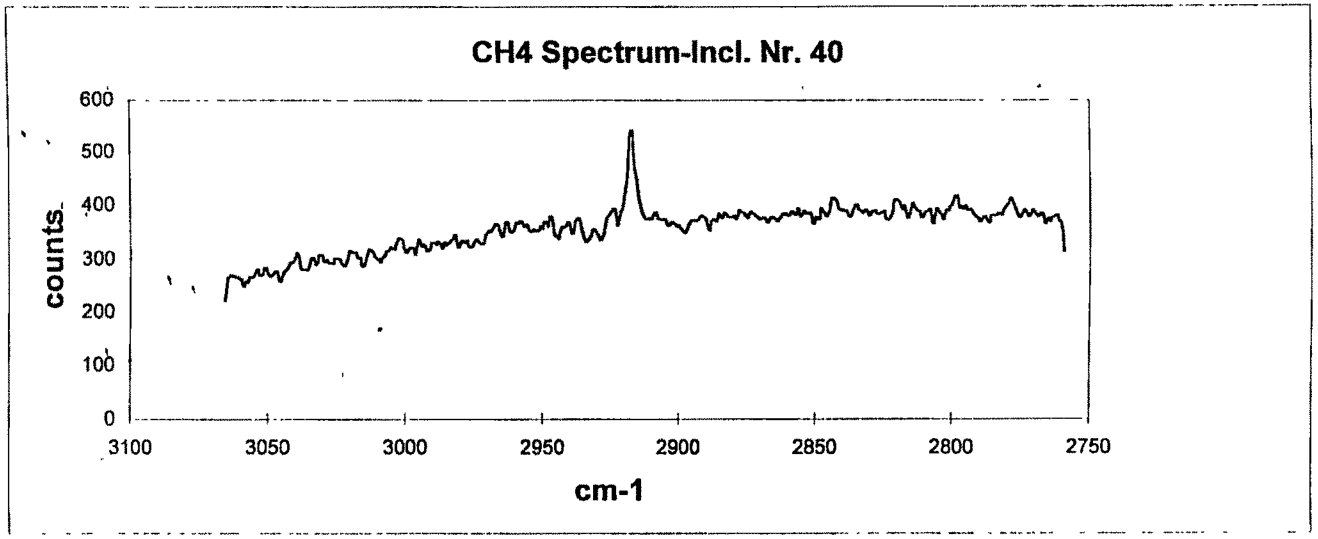

Fig. 7.23. Raman spectra for (a) CO_2, (b) N_2 and (c) CH_4. (a) and (b) belong to inclusion no. 32 and (c) is for inclusion no. 40 in table 7.7.

Type 7.7

Table showing data of fluid inclusions subjected to Raman microspectroscopy

Inclusion Type	Inclusion Nr.	T_m (°C)	T_h (°C)	CO_2 (%)	CH_4 (%)	N_2 (%)	V_m (cc/mole)
High density CO_2	33	-57.2	-34.2	95		5	41.52
	32	-57.2	-23.7	96		4	43.13
	35	-57.1	-5.7	93	2	5	48.22
	37	-57.1	-5.4	95	1	4	48.31
	8a	-56.9	20.0	95	1	4	63.29
	7	-57.1	20.3	90	1	9	89.93
Low density carobonic	39				3	97	
	40				100		
	A			89		11	
	C			70	30		
Aqueous	27			50	50		
	31	9.8		86	14		

the carbonic phase was determined using the program *HOMOGEN* developed by Bakker (1998, unpublished; personal communication). This program calculates liquid-vapour equilibria with published equations of state and transforms homogenization temperatures of fluid mixtures with known composition into densities or molar volumes.

Based on the results from Raman analysis for type-1 fluid inclusions which restrict the fluid composition of the carbonic phase to a binary CO_2-N_2 system, bulk molar volume and composition for the inclusions in this group were obtained by optical estimates from vX diagrams for CO_2-N_2 fluid system according to Thiéry et al. (1994). These diagrams allow a graphical interpretation of bulk fluid properties from the reduced melting temperatures of CO_2 and the homogenization temperature.

7.4.6. Discussion

Using the data from Table 7.3 for type-1 fluid inclusions, isochores (lines of equal density on a P-T diagram) were calculated with the aid of the program *ISOCHOR* written by Bakker (1998, unpublished; personal communication). It is generally accepted that the formation conditions of these fluid inclusions must lie along this line (e.g. Roedder, 1984). The compressibility and expansion of the host mineral is taken into account in these calculations, which is usually neglected in most other studies. Fig. 7.24 illustrates that the estimated pressure at higher temperatures may have been underestimated (> 1kbar) if the correction is not taken into account.

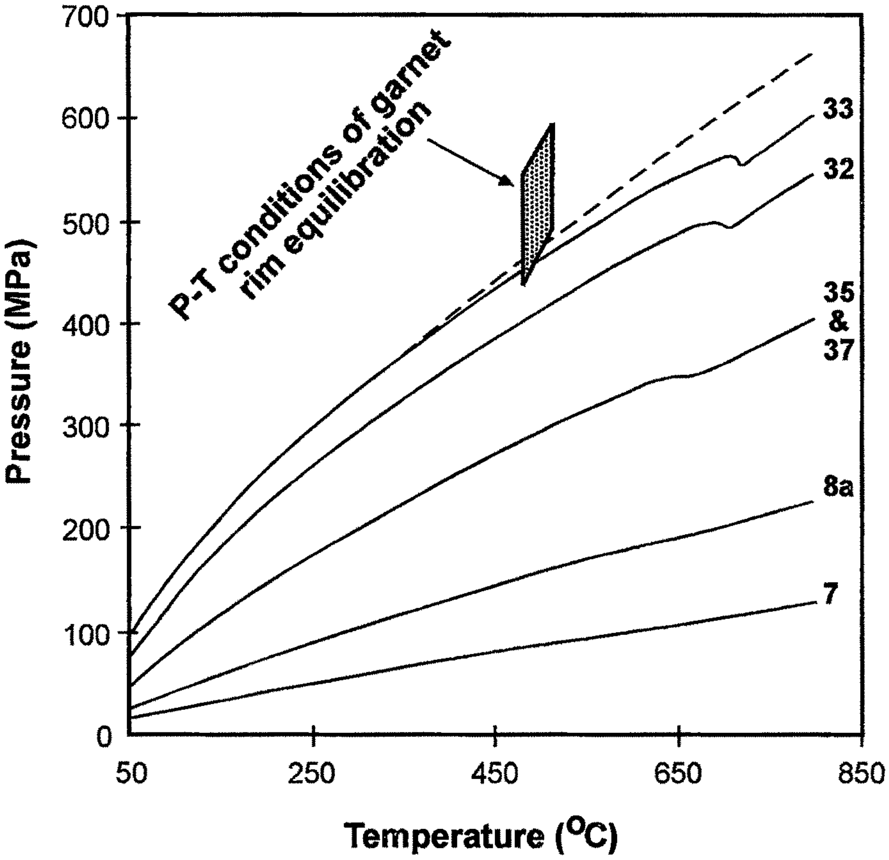

Fig. 7.24. Diagram showing the isochores for the CO_2 rich Type-1 fluid inclusions which were analyzed by Raman microspectroscopy. The Inclusion number is mentioned in front of each isochore. The dashed isochor is for inclusion number 33 without the correction for expansion of quartz. The isochore of inclusion number 33 passes through the rim P-T conditions of garnet which were determined through microprobe studies.

It is known that tectonic processes commonly terminate with a rapid uplift phase (Hollister, 1982; Selverstone, et. al. 1984; Crawford and Hollister, 1986). Fluid inclusion studies performed on the rocks from the Lunavada region presently investigated also provide similar results. The isochore for inclusion number 33 (Table 7.7) which has the minimum V_m (i.e. maximum density) shows the highest P-T conditions amongst the measured inclusions and this coincides with the P-T conditions of the rim of the garnet porphyroblast (Fig. 7.24) determined independently with the aid of thermobarometric studies (Section 7.3.2). This has led to the conclusion that inclusion number 33 and similar high density inclusions in the sample were entrapped at the garnet rim P-T conditions. The isochores for the other inclusions with lower densities pass through lower P conditions (Fig. 7.24). This indicates that the Type-1 fluid inclusions with decreasing densities were entrapped at lower P conditions or they were all formed at the garnet rim P-T conditions and subsequently re-equilibrated with the decreasing P conditions as the rocks were uplifted. It is important to mention here that the thermobarometric studies (Section 7.3) on this sample indicate release of pressure during growth of garnet from core to the rim, thus pointing to uplift during orogenesis. The range of densities from the fluid inclusions studied implies that this process of uplift continued even after the garnet rim P-T conditions had been achieved.

The timing of different types of inclusions also requires some discussion. As mentioned above, the high density CO_2 rich Type-1 fluids with upto 10 mole% N_2 were trapped at rim P-T conditions of the garnet. These inclusions occur as isolated clusters. All these facts imply that these inclusions are the oldest inclusions preserved in the rock. This inference is further supported by the petrographic observation that the inclusion trails comprising Type-2 and 3 inclusions cut across clusters of Type-1 inclusions at a few places. Moreover, the Type 3 inclusion trails also have big dark fluid inclusions which in all probability are the relicts of CO_2 rich type-1 fluid inclusions. These generally do not respond to freezing experiments upto -165°C. However, there is one inclusion (Incl. No. R79, Table 7.6) which homogenized in the vapour phase at -154°C . This appears to be an indication of the presence of a carbonic phase rich in CH_4 or N_2. It is envisaged that such inclusions formed by cracking/fracturing of the type-1 inclusions and were refilled by other fluids. All the above information implies that the formation/entrapment of type-2 and 3 occurred after that of Type-1 inclusions.

It can be argued that there is a possibility of loss of fluids from the Type-1 inclusions during decrepitation due to overpressure as the rocks were uplifted towards the surface of the earth. The graph of average diameter of fluid inclusion vs. T_h (Fig. 7.15) shows that smaller inclusions have higher densities and lower T_h. Experimental studies by Leroy (1979) and Bodnar et. al. (1989) have given a similar relation between inclusion size and decrepitation behaviour at 1 atmosphere confining pressure. Non-elastic deformation, i.e. decrepitation, resulted in fluid inclusion total volume increase which must lead to fluid density decrease if no fluid is lost from the system. Swanenburg (1980) observed this size effect in natural monophase carbonic inclusions in rocks from Faurefjell metasediments high grade metamorphic Pre-Cambrians of south-west Norway. He suggested that the relation between inclusion size and homogenization temperature reflects the enhanced mechanical strength of smaller sized inclusions during the post-entrapment period. Relatively large inclusions are more likely to undergo decrepitation and subsequent leakage. The trend in Fig. 7.15 indicates that similar processes could have taken place in these Type-1 fluid inclusions, although any morphological traces of decrepitation could not be detected. Ductile deformation of the inclusion walls might have been the most important process producing increased total volume of inclusions due to internal overpressures as illustrated by Bakker and Jansen (1994).

The presence of different types of fluids in single trails implies heterogeneous fluid trapping, i.e. two unmixed fluids were present during crack healing of the quartz. At the contact zone of these fluids, intermediate type of fluids might have been entrapped (Fig. 7.16). Heterogeneous trapping is a common process in any salt bearing system because the fluid immiscibility extends to extremely high temperatures and pressures. Type-2 fluid inclusions may have resulted from the introduction of a NaCl rich aqueous external fluid in the system containing the previously mentioned Type-1 fluid. Both type of fluids would quickly reach an equilibrium stage in which one end member is a salt-rich aqueous solution with minor amounts of gas and the other end member is a low density gas rich fluid with minor amounts of H_2O. The salt rich fluid could have been derived from hydrothermal solutions related to Godhra Granite intrusion.

During the formation of Type-3 inclusions, a completely different type of fluid must have intruded the system, with the previously mentioned NaCl-rich fluid having completely left the system. A new salt rich fluid intruded the system which must have had a completely different source because the salt is mainly $CaCl_2$ and has much higher salinities.

The timing of Type-4 fluid inclusions in relation to Type 1,2 and 3 inclusions is somewhat uncertain because this category comprises inclusions which were too small to be measured. The Type-4 inclusions occur along quartz grain boundaries. On the basis of CSD studies of quartz crystals in the schist presently investigated, Mamtani and Karanth (1996 b) have shown that the quartz crystals underwent considerable annealing; they correlated this feature with the heat supplied by the Godhra Granite (Section 6.8). Therefore, it is logical to interpret that the Type-4 fluid inclusions formed during the recrystallization of quartz crystals and this took place due to heat supplied by the granite. This would, in turn, imply that the fluids in the Type-4 inclusions were probably derived from the granite.